

ARMY RESEARCH LABORATORY



Navier-Stokes Computations for a Spinning Projectile From Subsonic to Supersonic Speeds

by Sidra I. Siltan

ARL-TR-2850

September 2002

Approved for public release; distribution is unlimited.

20021115 020

NOTICES

Disclaimers

The findings in this report are not to be construed as an official Department of the Army position unless so designated by other authorized documents.

Citation of manufacturer's or trade names does not constitute an official endorsement or approval of the use thereof.

Destroy this report when it is no longer needed. Do not return it to the originator.

Army Research Laboratory

Aberdeen Proving Ground, MD 21005-5066

ARL-TR-2850**September 2002**

Navier-Stokes Computations for a Spinning Projectile From Subsonic to Supersonic Speeds

Sidra I. Siltan

Weapons and Materials Research Directorate, ARL

Acknowledgments

The author wishes to thank J. Sahu for all the discussions and assistance in using the software and analyzing the data. This work was supported by a grant of computer time from the Department of Defense High Performance Computing Major Shared Resource Center at the U.S. Army Research Laboratory.

Contents

Acknowledgments	i
List of Figures	iii
List of Tables	iv
1. Introduction	1
2. Solution Technique	2
2.1 Numerical Techniques.....	2
2.2 Semi-Empirical Method	2
3. Model Geometry and Numerical Grid	3
3.1 Numerical Geometry and Grid.....	3
3.2 Semi-Empirical Geometry.....	7
4. Results and Discussion	7
4.1 Grid Resolution Study	7
4.2 Data Comparison	9
4.3 Flow Physics.....	14
4.3.1 Subsonic Flow	14
4.3.2 Transonic Flow	20
4.3.3 Supersonic Flow	23
5. Summary and Conclusions	28
6. References	29
Report Documentation Page	31

List of Figures

Figure 1. Sketch of .50-cal. projectile used for computational model. All dimensions are in calibers (1 cal. = 12.95 mm).	3
Figure 2. Three-dimensional (3-D) view of computational model.	3
Figure 3. Representative surface grid where sections are indicated by different colors.	4
Figure 4. Grid used for medium resolution supersonic CFD solutions.	5
Figure 5. Grid used for subsonic and low supersonic CFD solutions.	6
Figure 6. Grid used for transonic CFD solutions.	6
Figure 7. Geometry utilized in semi-empirical method (no groove, straight boattail).	7
Figure 8. Pressure coefficient contour comparison between (a) medium resolution and (b) fine resolution grids in the yaw angle plane.	9
Figure 9. Mach number contour comparison between (a) medium resolution and (b) fine resolution grids in the yaw angle plane.	10
Figure 10. Zero-yaw drag coefficient vs. Mach number data comparison.	11
Figure 11. Drag coefficient vs. Mach number data comparison.	11
Figure 12. Data comparison for lift force coefficient vs. Mach number.	12
Figure 13. Data comparison for static moment coefficient vs. Mach number.	12
Figure 14. Comparison of data for Magnus moment coefficient vs. Mach number for $\alpha = 2^\circ$	14
Figure 15. 155-mm artillery round (a) photo and (b) Magnus moment coefficient vs. Mach number for various AOAs [16].	15
Figure 16. Comparison of data for Magnus moment coefficient vs. Mach number for $\alpha = 5^\circ$	16
Figure 17. Mach number contours for $M = 0.70$, $\alpha = 0^\circ$, planar cut.	16
Figure 18. Pressure contours for $M = 0.70$, $\alpha = 0^\circ$, planar cut.	17
Figure 19. Mach number contours for $M = 0.70$, $\alpha = 2^\circ$, yaw plane.	18
Figure 20. Pressure contours for $M = 0.70$, $\alpha = 2^\circ$, yaw plane.	18
Figure 21. Mach number contours for $M = 0.70$, $\alpha = 2^\circ$, non-yaw plane.	19
Figure 22. Pressure contours for $M = 0.70$, $\alpha = 2^\circ$, non-yaw plane.	19
Figure 23. Pressure contours for $M = 0.98$, $\alpha = 0^\circ$, planar cut.	21
Figure 24. Mach number contours for $M = 0.98$, $\alpha = 0^\circ$, planar cut.	21
Figure 25. Mach number contours for $M = 0.98$, $\alpha = 2^\circ$, non-yaw plane.	22
Figure 26. Pressure contours for $M = 0.98$, $\alpha = 2^\circ$, non-yaw plane.	22
Figure 27. Pressure contours for $M = 0.98$, $\alpha = 2^\circ$, yaw plane.	23

Figure 28. Mach number contours for $M = 0.98$, $\alpha = 2^\circ$, yaw plane.....	24
Figure 29. Mach number contours for $M = 2.0$, $\alpha = 0^\circ$, planar cut.	25
Figure 30. Pressure number contours for $M = 2.0$, $\alpha = 0^\circ$, planar cut.....	25
Figure 31. Mach number contours for $M = 2.0$, $\alpha = 2^\circ$, non-yaw plane.	26
Figure 32. Pressure contours for $M = 2.0$, $\alpha = 2^\circ$, non-yaw plane.	26
Figure 33. Mach number contours for $M = 2.0$, $\alpha = 2^\circ$, yaw plane.....	27
Figure 34. Pressure contours for $M = 2.0$, $\alpha = 2^\circ$, yaw plane.....	28

List of Tables

Table 1. Mach numbers and resulting roll rates used in CFD calculations.	8
Table 2. Grid resolution study at $M = 2.7$, $\alpha = 0^\circ$	8
Table 3. Grid resolution study at $M = 2.7$, $\alpha = 2^\circ$	10

1. Introduction

Many U.S. Army projectiles are slender, spinning bodies. When flown at an angle of attack (AOA), these projectiles are then subject to Magnus forces and moments. Although these forces are generally quite small (10–100 times smaller than the normal force) and can usually be ignored, the moment produced by these forces is critical in determining the stability of the projectile. Thus, it is important to be able to accurately determine these coefficients.

Early numerical studies that have looked at spinning projectiles [1–3] have suffered from a number of problems. The supersonic flow study [1] seemed to have produced fairly good results using the Parabolized Navier-Stokes equations. However, the grid resolution was probably questionable due to the computational resources available. The 1983 transonic study [2] also produced questionable results due to inadequate grid resolution caused again by limited computational resources. While the 1991 study [3] was able to utilize a much better grid and more robust supercomputers, a very limited number of Mach number and AOA were investigated. As the computational fluid dynamics (CFD) software and computational resources improve, more complete and accurate numerical aeroballistics data can be obtained. The present study was undertaken in order to verify the ability of a relatively new CFD software package to predict this more complete aeroballistics data for a spinning projectile. This particular CFD software has been previously used to calculate the flow fields and resulting aeroballistics data on nonspinning projectiles [4], but had not yet been benchmarked for a spinning projectile and the associated force and moment (i.e., Magnus force and moment). Prior to using this software to determine aeroballistics data for new spinning projectile designs, the software must be verified against existing data and methods to determine its accuracy.

The .50 cal. projectile has been in use for almost 60 years. While a limited amount of aerodynamic data was collected during the projectile's development and testing [5], a relatively large amount of aerodynamic data has been obtained over the years for these rounds. Most of the data have been collected within the last 15 years at the U.S. Army Research Laboratory's (ARL) Free Flight Aerodynamics Range* [6]. Parabolized Navier-Stokes numerical aeroballistics data have also been obtained for a similarly shaped .50-cal. training round with fairly good results [7].

The numerical aeroballistics data obtained in this study are compared to existing range data as well as semi-empirically obtained aerodynamic coefficients. The flow field of the spinning projectile is then examined within each flow regime investigated.

* Formerly the U.S. Army Ballistic Research Laboratory Free Flight Aerodynamics Range.

2. Solution Technique

2.1 Numerical Techniques

CFD++ Solver Software [8] (Metacomp Technologies) was utilized for this study. CFD++ solves the Reynolds-averaged Navier-Stokes equations with pointwise turbulence models. The equations are solved within a finite volume framework using an unstructured grid topology. Spatial discretization is accomplished using the cell face normal at the cell face centroid, which is obtained by reconstructing the cell centroid values. Both implicit and explicit time integration schemes are available. For the present study, the point-implicit integration scheme was used to solve the steady-state simulation. Ramping of the Courant number allowed for quicker solution convergence as the flow progressed toward solution, and larger time steps had less effect on the solution. CFD++ also allows for turbulence modeling. For the study presented herein, the pointwise k - ϵ (epsilon) turbulence model [9] was used.

All boundary conditions have been explicitly imposed. The far field and inflow boundaries are set to free stream condition. The outflow boundary is set to have free stream conditions for subsonic outflow and to extrapolate from the previous cell if the outflow is supersonic. Free stream pressure and temperature are set to 101 kPa and 288 K, respectively. Density can then be calculated from the perfect gas assumption. For the projectile body, the boundary condition is set to be a no slip, isothermal wall (at 288 K) that is rotating about the x-axis. The projectile rotates at a speed corresponding to the rifling twist rate of the experiments [6] of 1 turn in 38.1 cm.

2.2 Semi-Empirical Method

The semi-empirical solution was obtained using AP98 code [10] (Aeroprediction Inc.). AP98 combines a large database of experimental results and well-verified numerical results with theoretical methods in order to obtain aerodynamic coefficients and dynamic derivatives. The theoretical methods include second-order van Dyke and second-order shock expansion theory as well as thin wing theory and slender body assumptions. It allows coefficients to be obtained in a relatively short period of time within engineering accuracy as no grid is needed.

3. Model Geometry and Numerical Grid

3.1 Numerical Geometry and Grid

The computational model is a .50-cal. (1 cal. = 12.95 mm) projectile, 4.46 cal. in length with a .16-cal.-long, 0.02-cal.-deep groove, and a 9° filleted boattail [6] (see Figures 1 and 2). A center of gravity location of 2.68 cal. (34.706 mm) from the nose tip was utilized.

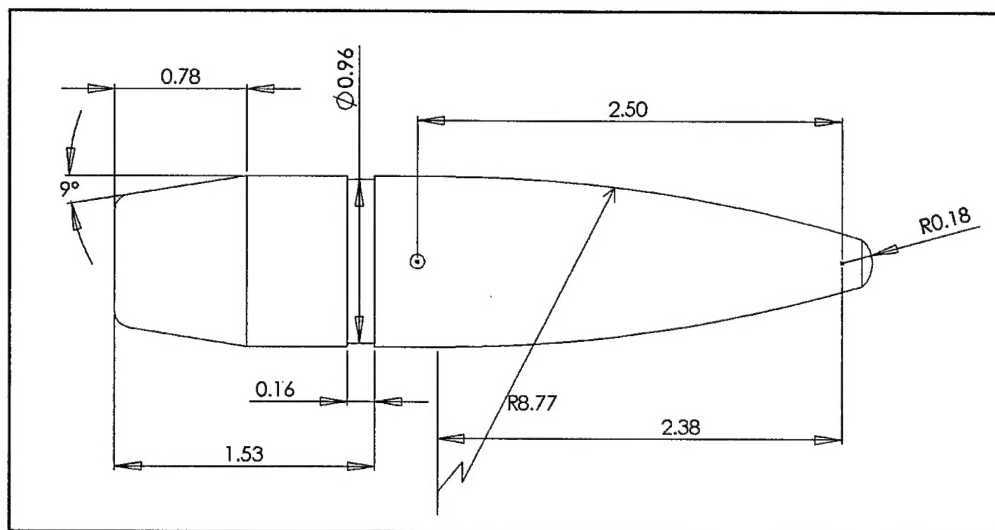


Figure 1. Sketch of .50-cal. projectile used for computational model. All dimensions are in calibers (1 cal. = 12.95 mm).

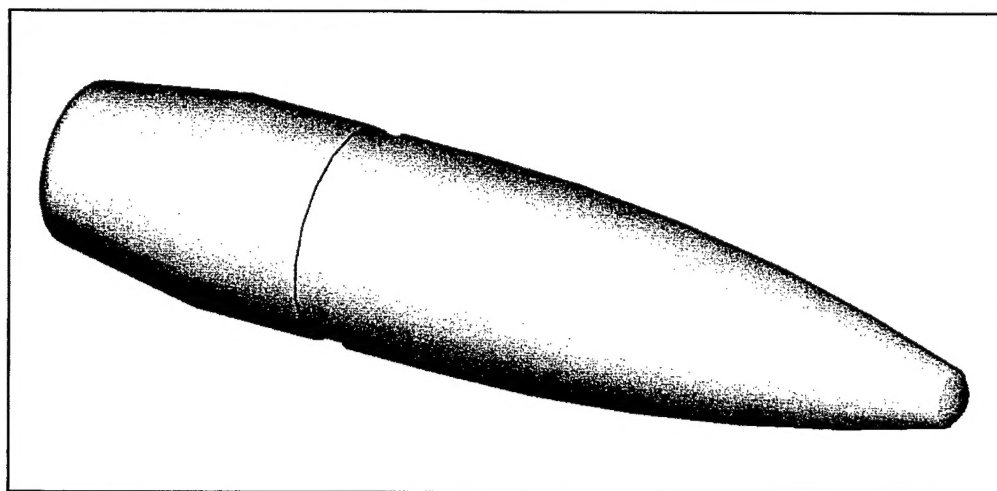


Figure 2. Three-dimensional (3-D) view of computational model.

All grids used in this study were 3-D hexahedral meshes created using GRIDGEN Version 13 software [11] (Pointwise Inc.). The grid is created in a multiblock format in order to allow for a better quality mesh and then written in an unstructured format. While GRIDGEN Version 13 does not output meshes in CFD++ format, FLUENT Version 5 software [12] (Fluent Inc.) output format is available, which CFD++ is able to import.

Four separate meshes were constructed over the course of this study: one for subsonic and low supersonic cases, one for a near-sonic case, and two for supersonic cases. Two different computational grids were created for the supersonic cases in order to verify grid independence. In each case, the far field boundary was created so that it would not interfere with the flow field in the regime investigated (subsonic, transonic, and/or supersonic).

The mesh is composed of 10 structured blocks. The surface grid (Figure 3) was generated first and consists of four sections: two small squares (pink) projected on the nose and base to eliminate singularities on the symmetry axis, the groove (red), and the remainder of the body (blue). After constructing a companion far field grid, radial planes were constructed between these two surface grids in order to create 3-D blocks. Two of these blocks are small rectangular blocks beginning at the small projected squares on the nose and base of the body and extending to the outer boundary (each 30×30 cells on the body), with the axial dimension equal to the radial dimension of the remaining flow field. The rest of the body is divided into quadrants based on the corners of the surface squares, with the groove blocked separately. Each quadrant of the groove contains 30 radial cells, 30 circumferential cells, and 18 axial cells, while each quadrant for the remainder of the flow field varied with the position of the far field boundary. In order to accurately capture the flow in the turbulent boundary layer, the first radial surface spacing was always set to $1.07 \mu\text{m}$.

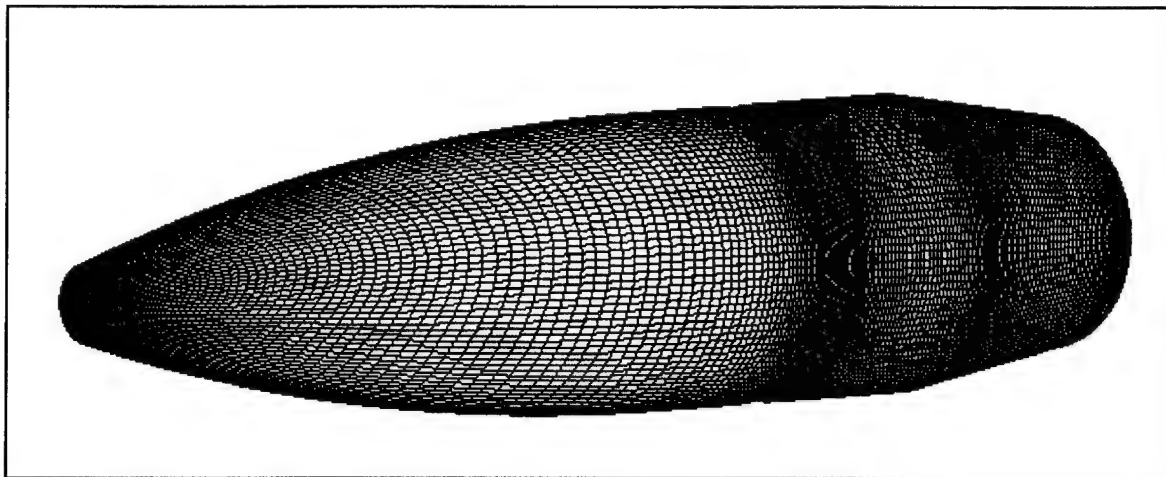


Figure 3. Representative surface grid where sections are indicated by different colors.

For both supersonic grids, the outflow boundary was two body lengths behind the base of the model, the inflow boundary was just over one body length in front of the model, and the circumferential boundary was also just over one body length away from the model (Figure 4). The medium resolution grid contained 30 circumferential cells, 80 radial cells (away from the body), and 279 cells along the body surface and far field boundary in one quadrant (2,737,658 cells total) while the finer resolution grid contained 30 circumferential cells, 150 radial cells, and 296 cells along the body surface in one quadrant (5,413,314 cells total). The additional radial cells were added near the surface so that the boundary layer cell thickness grew more slowly. The additional axial cells were added in the nose and base regions. The greater number of cells in the radial and axial directions for the finer grid allowed finer details of the flow field to be studied.

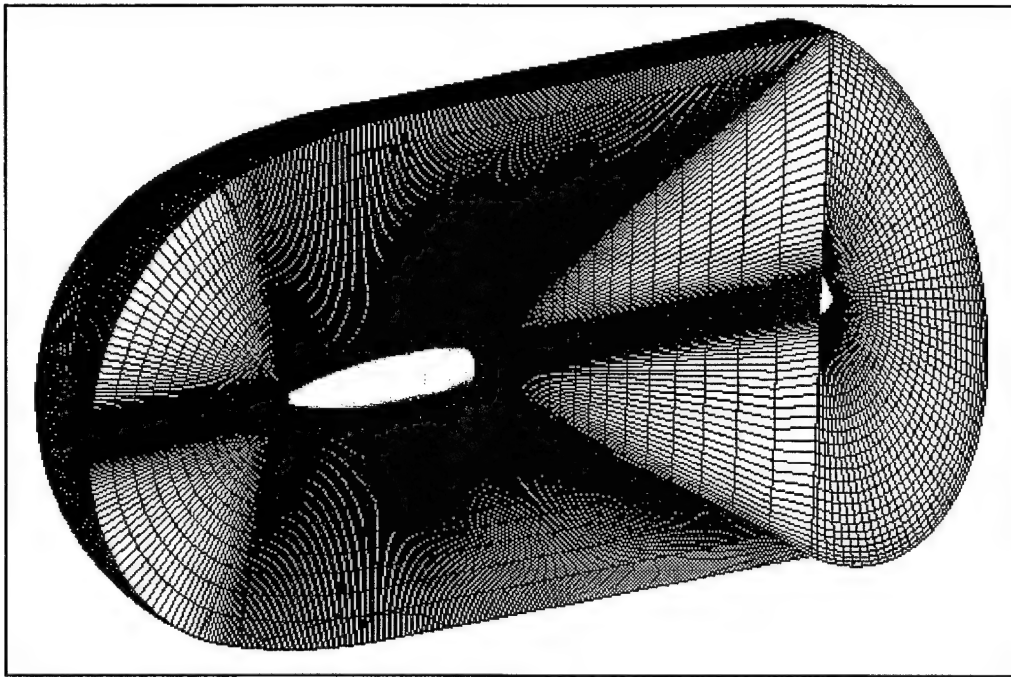


Figure 4. Grid used for medium resolution supersonic CFD solutions.

The mesh created for the subsonic and low supersonic cases was similar in structure to that created for the supersonic case. The far field boundary was moved farther away from the projectile body (Figure 5) to accommodate the weaker shocks, expansions, and longer recovery distances of flow field features. The new inflow boundary was located just under three body lengths away, the outflow boundary four body lengths away, and the circumferential boundary almost five body lengths away. While the circumferential dimension remained constant at 30 cells in one quadrant, the radial dimension was increased to 100 cells and the axial dimension to 289 cells in order to accommodate the new position of the far field boundary. The cells were again added on the nose and the base of the projectile. The complete mesh consisted of 3,712,800 cells.

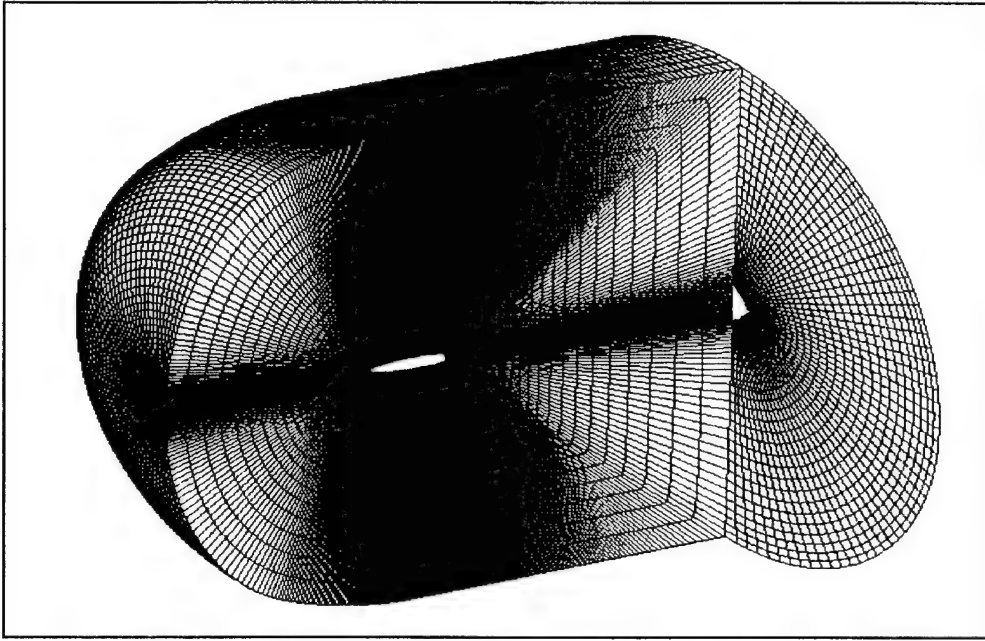


Figure 5. Grid used for subsonic and low supersonic CFD solutions.

Due to the near-normal shock and large recovery distances of a near-sonic flow, a special grid was constructed for this case. The grid further distanced the far field boundary from the body and added additional cells in the radial direction (Figure 6). Specifically, the outflow boundary was expanded to eight body lengths downstream and the circumferential boundary was expanded to almost 10 body lengths away. The resulting grid contained 30 circumferential cells, 289 axial cells, and 109 radial cells in each quarter mesh. This increased the total mesh size to 4,041,120 cells.

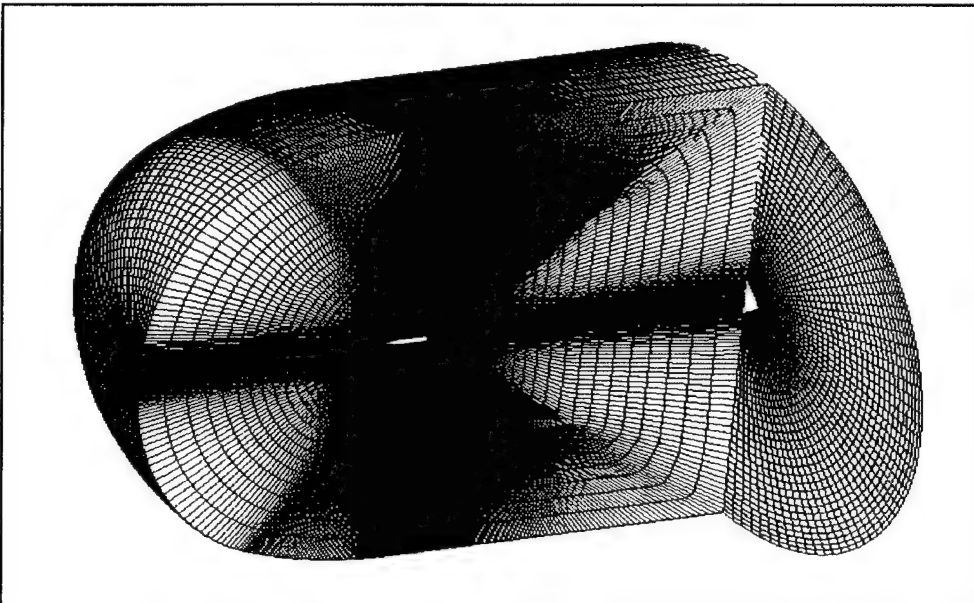


Figure 6. Grid used for transonic CFD solutions.

3.2 Semi-Empirical Geometry

The assumptions within the semi-empirical solution all pertained to the afterbody geometry due to limitations of the software. First, the groove was eliminated as a decrease in body radius followed by a subsequent increase could not be handled by the software. Additionally, the filleted boattail was eliminated and replaced with a standard 9° angle boattail. These modifications to the geometry produced a model with the cross section in Figure 7 and allowed for a solution to be calculated. The center of gravity for the semi-empirical solution was assumed to be that of the experimental model with the groove and filleted boattail.

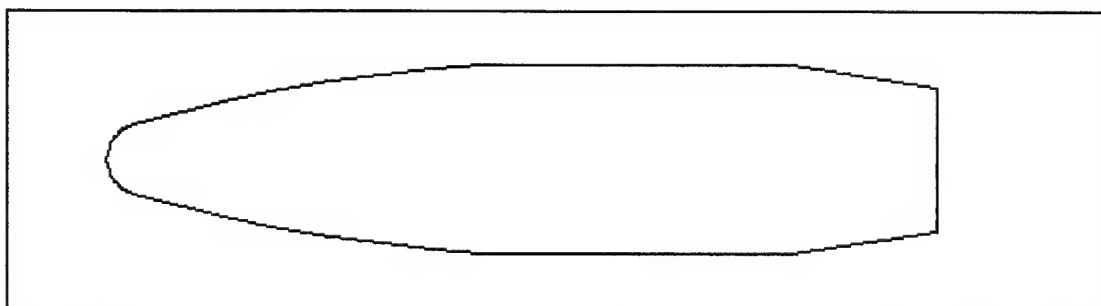


Figure 7. Geometry utilized in semi-empirical method (no groove, straight boattail).

4. Results and Discussion

A number of numerical cases were studied in order to cover the range of experimental data available. The Mach numbers and corresponding roll rates can be found in Table 1. A CFD calculation was completed for each Mach number at 0° and 2° AOA. The dynamic aerodynamic coefficients were calculated assuming that the values at 0° AOA were zero. Only C_{D0} was obtained directly from the 0° AOA calculation. A limited number of CFD calculations were also completed at 5° AOA in order to determine how the coefficients changed. Solutions for the semi-empirical code were obtained at 2° AOA for the static coefficients. The dynamic derivatives were determined at 5° AOA. All results are presented in the convention put forth by Murphy [13].

4.1 Grid Resolution Study

A grid resolution study was conducted for the supersonic, $M = 2.70$, case at both 0° and 2° AOA. This case has the thinnest boundary layers and the most distinct flow physics for comparison. The solutions on the 2.7 million cell (medium) and 5.4 million cell (fine) grids were compared for differences in flow physics and aerodynamics coefficients, as well as for agreement with experimental data.

Table 1. Mach numbers and resulting roll rates used in CFD calculations.

Mach No.	Roll Rate (rad/s)
0.70	3927.9
0.85	4768.5
0.90	5050.3
0.94	5274.7
0.98	5499.2
1.05	5892.0
1.10	6172.5
1.25	7014.2
1.50	8417.0
2.00	11222.8
2.70	15150.6

At 0° AOA, the medium and fine grids gave nearly identical results with values very near zero for all coefficients, except the drag coefficient, C_D , as expected (Table 2). C_D differed by less than 1% and the flow fields were very similar. Experimental data are only available for C_D , as all other coefficients are 0 at 0° AOA.

Table 2. Grid resolution study at $M = 2.7$, $\alpha = 0^\circ$.

Grid/Experiment	C_D	C_L	C_N	$C_{M\dot{\alpha}}$	C_M
Medium grid	0.2935	-1.33e-5	1.49e-4	-0.0011	2.45e-4
Fine grid	0.2964	2.80e-5	2.23e-5	0.0004	8.33e-5
M33 experiment [6]	0.279	—	—	—	—

When the AOA is increased to 2° , the flow gets more complicated. The flow is no longer axisymmetric. The flow around the body was nearly identical between the two grids (Figures 8 and 9), although some of the flow features were better defined on the fine grid. Most of the aerodynamic coefficients, including Magnus moment coefficient, differed by no more than 0.5% (Table 3). Only C_D and the normal force coefficient, $C_{N\alpha}$, differed to a greater extent. C_D increased by just over 1% from the medium grid to the fine grid and $C_{N\alpha}$ increased by $\sim 10\%$.

Both sets of numerical results agreed quite well with the experimental data. While the agreement was slightly better with the fine grid, it was not worth the nearly doubled computational time that was required in order to obtain a converged solution on the fine grid as compared to that for the medium grid. As such, the medium grid was utilized for the remainder of the supersonic cases, and comparable grids were used for the transonic and subsonic cases.

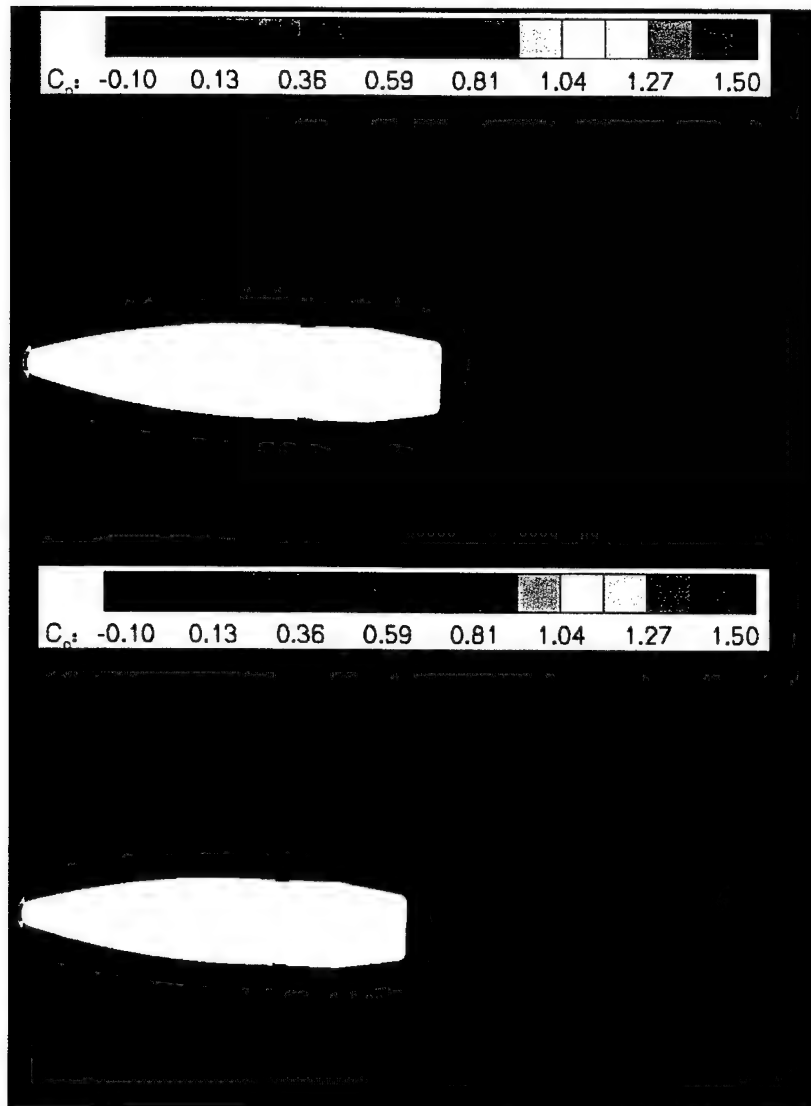


Figure 8. Pressure coefficient contour comparison between (a) medium resolution and (b) fine resolution grids in the yaw angle plane.

4.2 Data Comparison

All experimental data used in this data comparison were obtained in the ARL Aerodynamics Range [6]. Although experimental data were obtained for three different rounds, only the data for the M33 ball projectile (M33 experiment) and the M8 API projectile (M8 experiment) were used where they were available. Plotted experimental data are limited to $1^\circ < \alpha \leq 5^\circ$ because smaller yaw angles were unavailable and in order to eliminate large yaw angle nonlinearities in the analysis as the CFD results were obtained at small α [7]. The zero-yaw drag force coefficient, C_{D0} , was compared first. As expected, very good agreement was obtained between the computational results and the experimental results (Figure 10). It is interesting to note that while the numerical solution overpredicts the experimental C_{D0} results, the semi-empirical

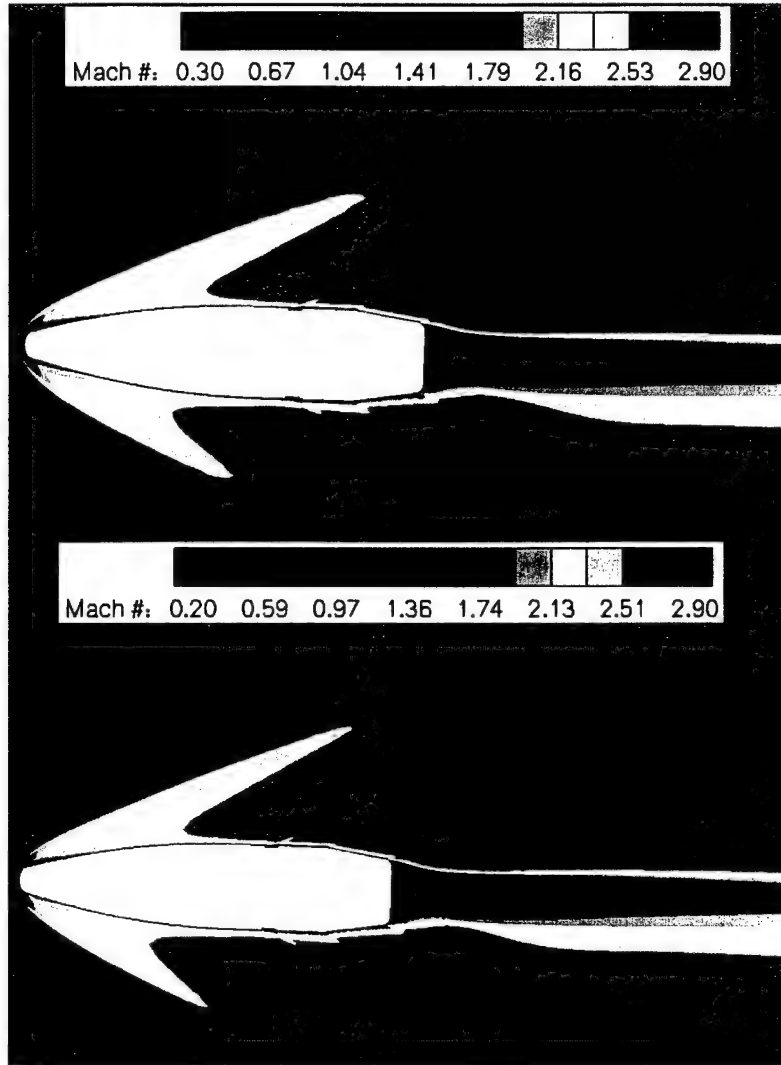


Figure 9. Mach number contour comparison between (a) medium resolution and (b) fine resolution grids in the yaw angle plane.

Table 3. Grid resolution study at $M = 2.7$, $\alpha = 2^\circ$.

Grid/Experiment	C_D	$C_{L\alpha}$	$C_{N\alpha}$	$C_{M_{p\alpha}}$	$C_{M\alpha}$
Medium grid	0.3027	2.23	0.0637	0.21	2.79
Fine grid	0.3062	2.23	0.0710	0.21	2.80
M33 experiment [6]	0.2813	2.21	—	0.15	3.01
M8 experiment [6]	0.2991	2.42	—	0.24	2.85

Note: Experimental data given at closest data point.

solution underpredicts them. Actual drag coefficient, C_D , was also compared (Figure 11) and shown to be in good agreement. Numerical drag appears to be a bit high, but could be accounted for in that the AOAs are not quite the same. Lift force coefficient, $C_{L\alpha}$ (Figure 12), and static moment coefficient, $C_{M\alpha}$ (Figure 13), were also directly compared to experimental data with much success. This indicates that the CFD is correctly predicting the aerodynamic coefficients.

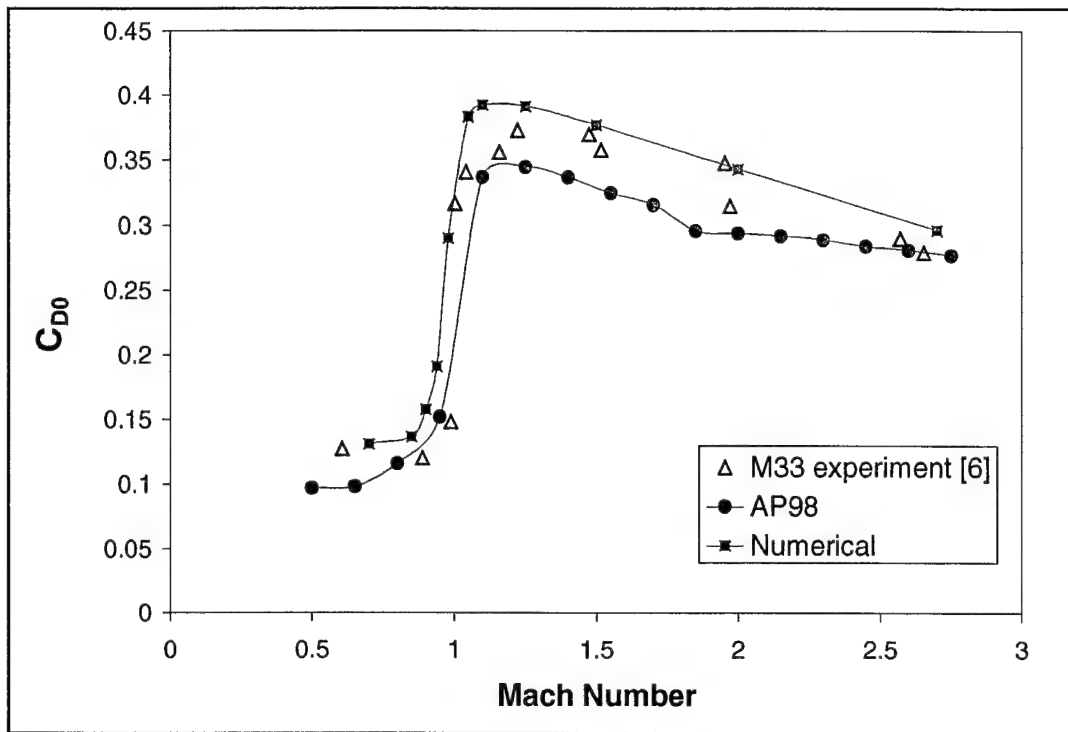


Figure 10. Zero-yaw drag coefficient vs. Mach number data comparison.

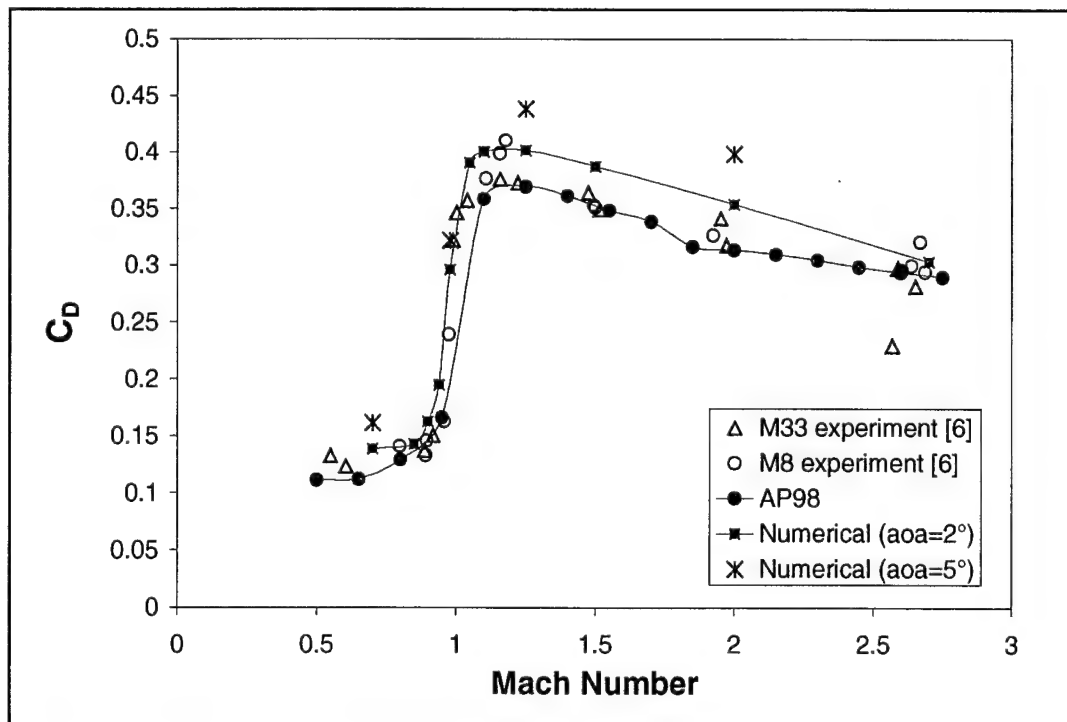


Figure 11. Drag coefficient vs. Mach number data comparison.

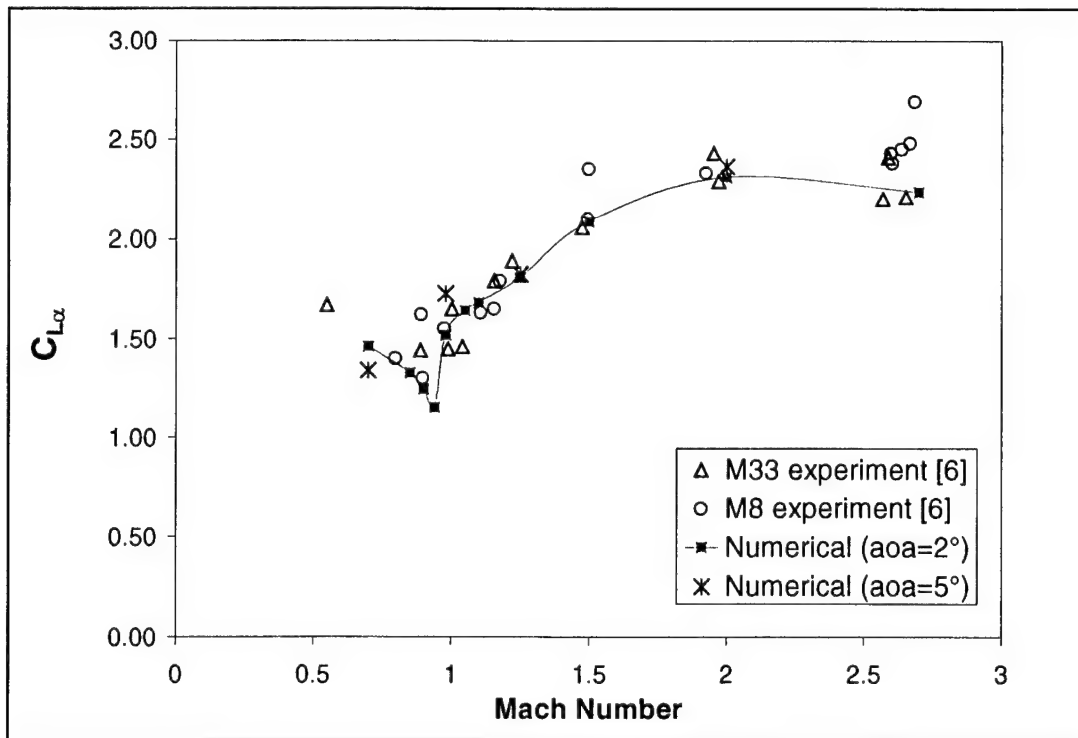


Figure 12. Data comparison for lift force coefficient vs. Mach number.

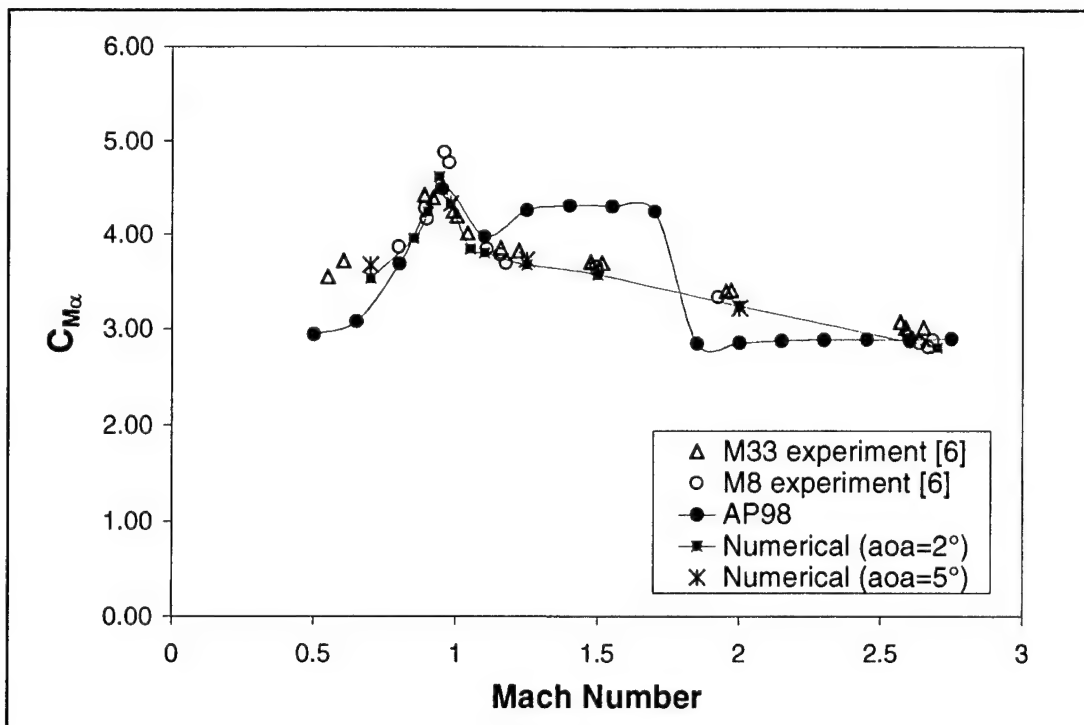


Figure 13. Data comparison for static moment coefficient vs. Mach number.

The discontinuity in the AP98 results in Figure 13 at Mach 1.6 is due to the theory used to calculate the coefficients changing. Aerodynamic coefficients are not much affected by body roll, however, and were expected to be in good agreement as this CFD code had been used many times previously with excellent results. The question here was how well the dynamic derivatives would match those of the experiment.

Unfortunately, due to the way in which the CFD was conducted (i.e., fixed boundary conditions), two of the dynamic derivatives—roll damping moment and pitch damping moment—could not be obtained. The Magnus moment coefficient, $C_{M_{p\alpha}}$, could be obtained, as the rotating wall boundary condition was utilized. As a range of AOAs was investigated experimentally, it was important to extrapolate the experimental data to the AOAs investigated numerically. The $C_{M_{p\alpha}}$ was plotted vs. effective square yaw by McCoy [6] for a given Mach number range for the combined M33 and M8 data. This shows that even at $\alpha = 2^\circ$, $C_{M_{p\alpha}}$ has a nonlinear component. The M33 and M8 data have recently been re-reduced [14] using the newer range reduction software, ARFDAS [15]. The result of the multiple data fit using this software is also presented here. At $\alpha = 2^\circ$ (Figure 14), agreement between the experimental and numerical data appears to be fair to good in the subsonic regime and the higher supersonic regime. However, agreement between the different experimental data sets is not very good in the transonic regime. This can be attributed to the differences that occur in the engraving of the rounds during rifling as the rounds are made of different materials. The complete lack of engraving on the numerical model could account for the disagreement with the experimental results in the transonic regime as well as in the lower supersonic regime. In fact, if one compares the shape of the Magnus moment coefficient curve obtained experimentally for the 155-mm artillery round [16] at $\alpha = 2^\circ$ (Figure 15) to that obtained numerically for the .50-cal. round at $\alpha = 2^\circ$ (Figure 14), they are nearly identical. This further substantiates the hypothesis that the engraving on the projectile surface does affect the Magnus moment coefficient. These effects are less pronounced at $\alpha = 5^\circ$ where the data trends in the numerical and experimental data appear to agree rather well (Figure 16). As only a few numerical data points were obtained, it is possible that the peak value in the transonic regime was not calculated. Agreement in the subsonic and supersonic regime is again quite good. The semi-empirical results (obtained from AP98 [10]) agree with the numerical and experimental data at $\alpha = 5^\circ$ in the subsonic regime, appear to split the difference near Mach 1, and overpredict the results in the supersonic regime. Again, the data trend is the same with the maximum coefficient being obtained very near Mach 1.

Based on comparison to experimental and semi-empirical data, the CFD is found to accurately predict the aerodynamic coefficients and limited dynamic derivatives. As such, this CFD solver should be able to accurately predict the flow physics.

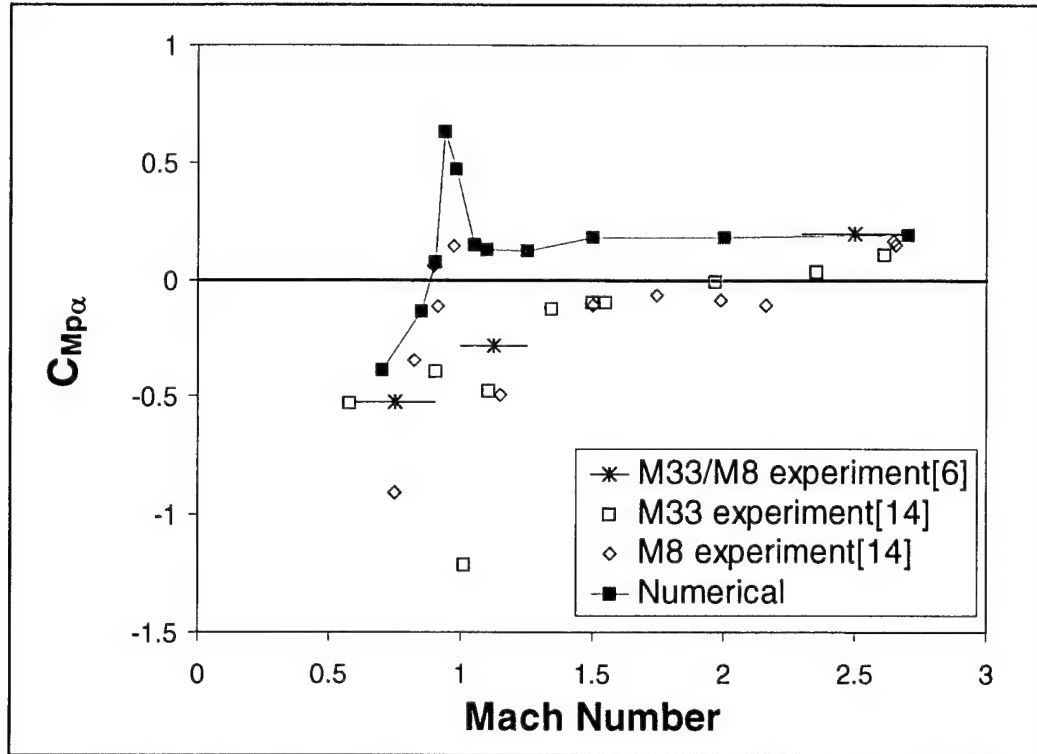


Figure 14. Comparison of data for Magnus moment coefficient vs. Mach number for $\alpha = 2^\circ$.

4.3 Flow Physics

The Mach numbers investigated encompass three projectile flight regimes: (1) subsonic, (2) transonic, and (3) supersonic. Because each flight regime has different flow characteristics, they are discussed separately. Because the flows at $\alpha = 2^\circ$ and $\alpha = 5^\circ$ are similar, only the $\alpha = 0^\circ$ and $\alpha = 2^\circ$ flows are discussed.

4.3.1 Subsonic Flow

Only one case, Mach 0.70, falls completely within the subsonic regime, as the flow remains less than Mach 1 everywhere along the body (Figure 17). Figure 17 shows the computed Mach contours and indicates that the flow at $\alpha = 0^\circ$ is an axisymmetric flow. As expected, a small stagnation region is present at the nose tip. A lower velocity bubble (less than free stream) exists upstream of the stagnation region because this is a subsonic flow and the flow is anticipating the body. The flow is turned as it moves around the body, but remains everywhere subsonic. Additionally, the flow in the groove is nearly stagnant. The flow then expands and separates as it passes the boattail. This creates a low-velocity, nominal pressure region of base flow (Figure 18). The pressure contours confirm the axisymmetric nature of the flow.

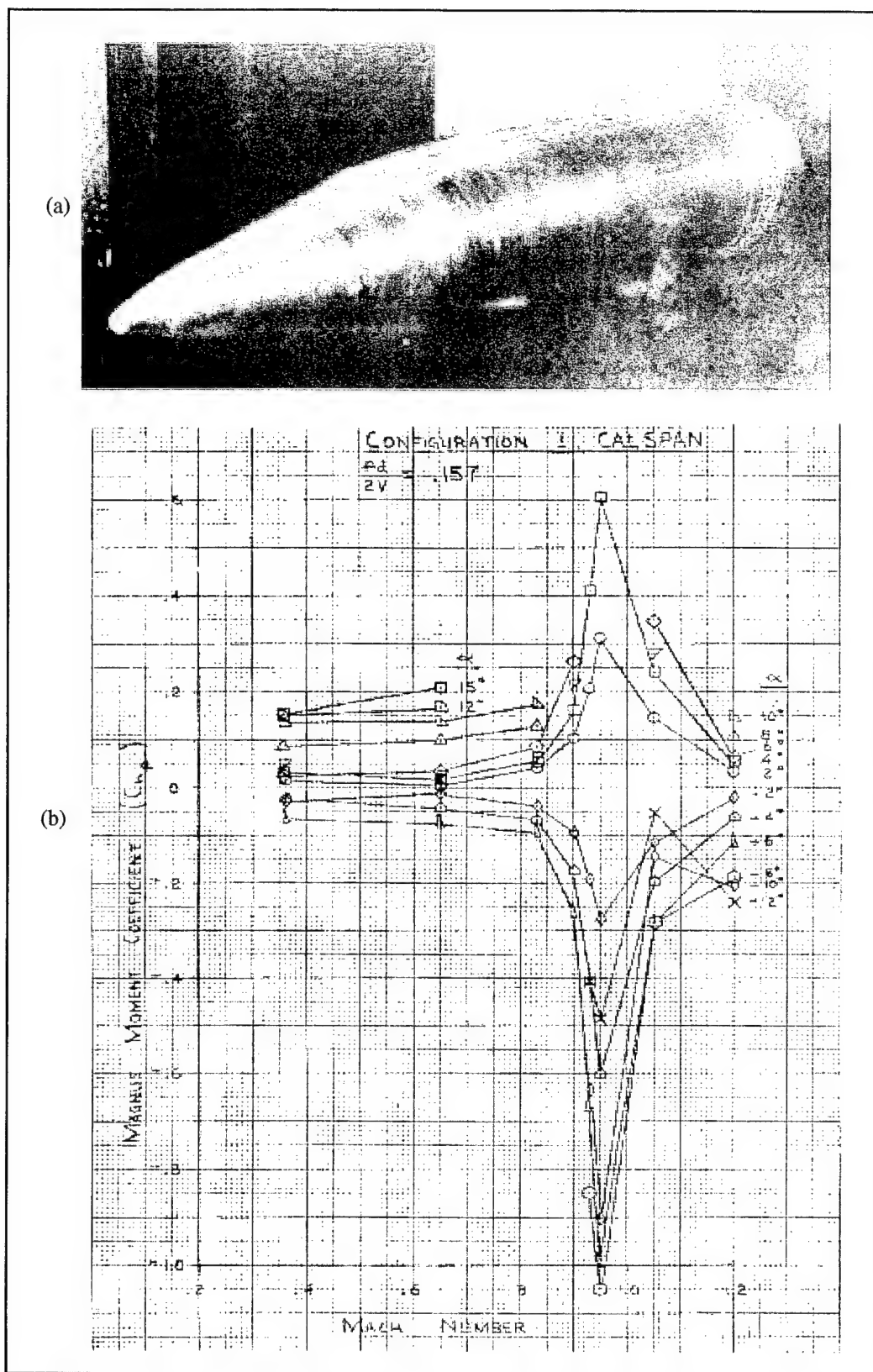


Figure 15. 155-mm artillery round (a) photo and (b) Magnus moment coefficient vs. Mach number for various AOAs [16].

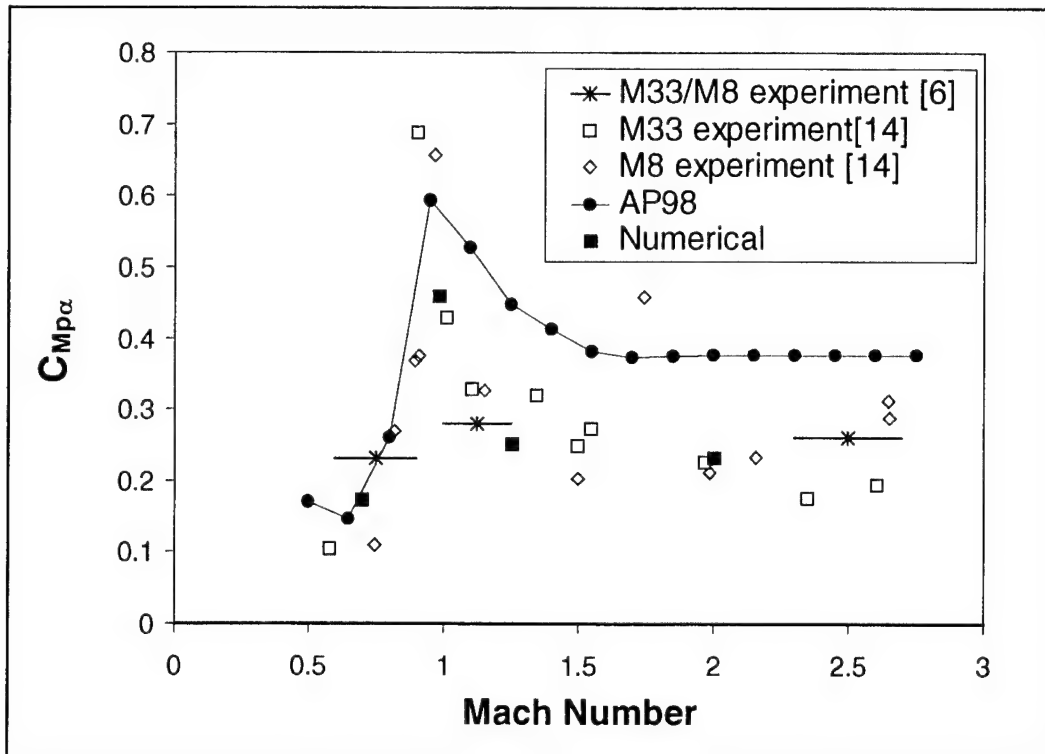


Figure 16. Comparison of data for Magnus moment coefficient vs. Mach number for $\alpha = 5^\circ$.

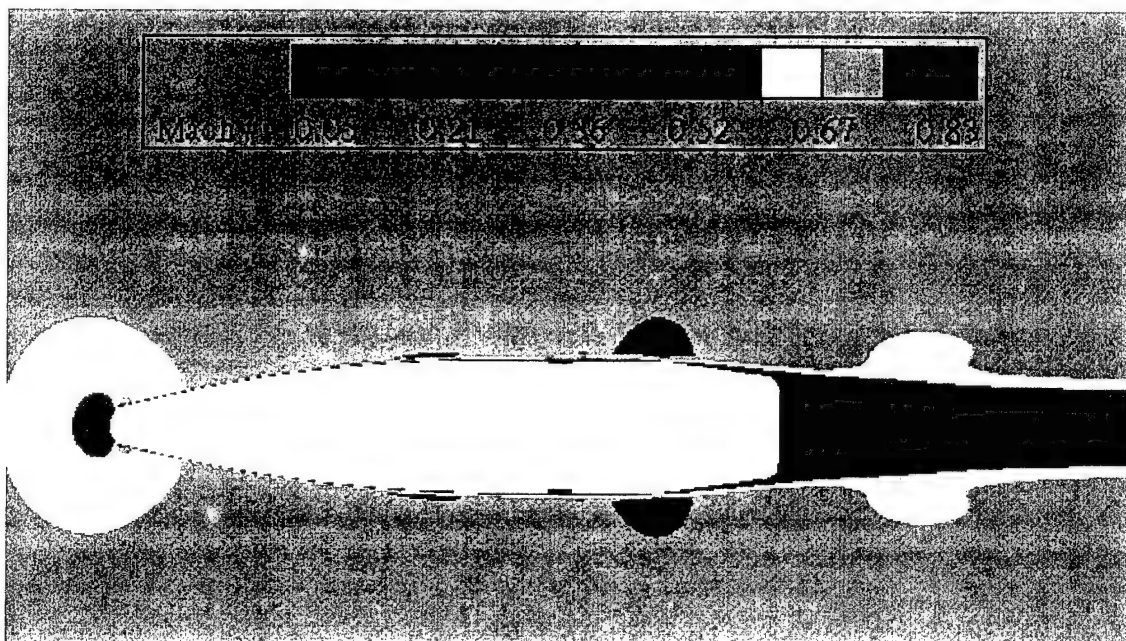


Figure 17. Mach number contours for $M = 0.70$, $\alpha = 0^\circ$, planar cut.

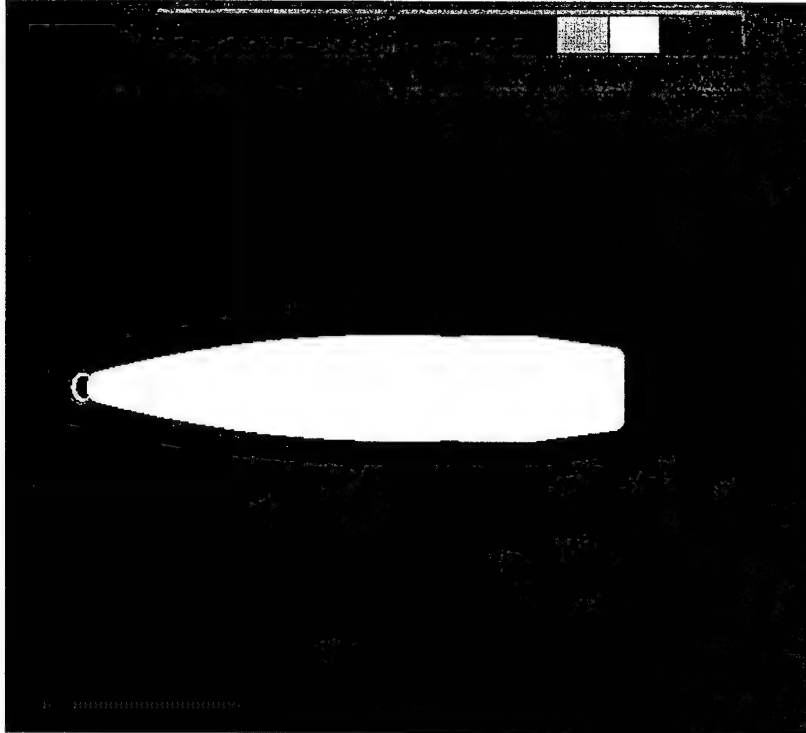


Figure 18. Pressure contours for $M = 0.70$, $\alpha = 0^\circ$, planar cut.

At $\alpha = 2^\circ$, the flow becomes asymmetrical as can be observed from the Mach number contours in the yaw angle plane (Figure 19). The asymmetry is not so obvious in the nose tip region, but becomes much more apparent as the flow moves along the ogive. A smaller adverse pressure gradient on the leeward side (Figure 20) allows the Mach number to increase more quickly and stabilize as the air moves past the groove. As the air reaches the angled boattail, a greater expansion angle is necessary on the leeward side (as the flow is at a 2° angle up) and the flow appears to separate. On the windward side, the turning angles are not as large, and the flow is allowed to expand, causing a region of high subsonic flow on the windward side of the boattail. The asymmetry in the velocity field decreases as one progresses away from this plane, except in the base flow region, and reaches a minimum in the non-yaw plane (Figure 21). A close look at the pressure contours (Figures 20 and 22) reveals some slight asymmetry in the low-pressure areas near the body in both planes. In the yaw angle plane (Figure 20), the higher pressure on the windward side of the body and lower pressure on the leeward side of the body account for the lift that is generated. The slightly unbalanced pressure regions in the non-yaw plane (Figure 22) accounts for the non-zero, though extremely small, side force and Magnus moment.

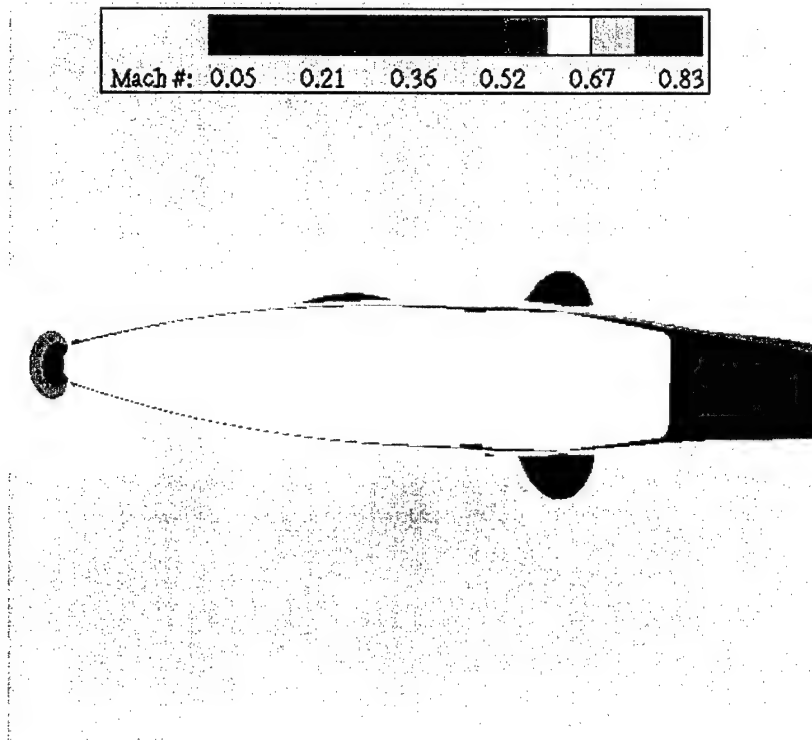


Figure 19. Mach number contours for $M = 0.70$, $\alpha = 2^\circ$, yaw plane.

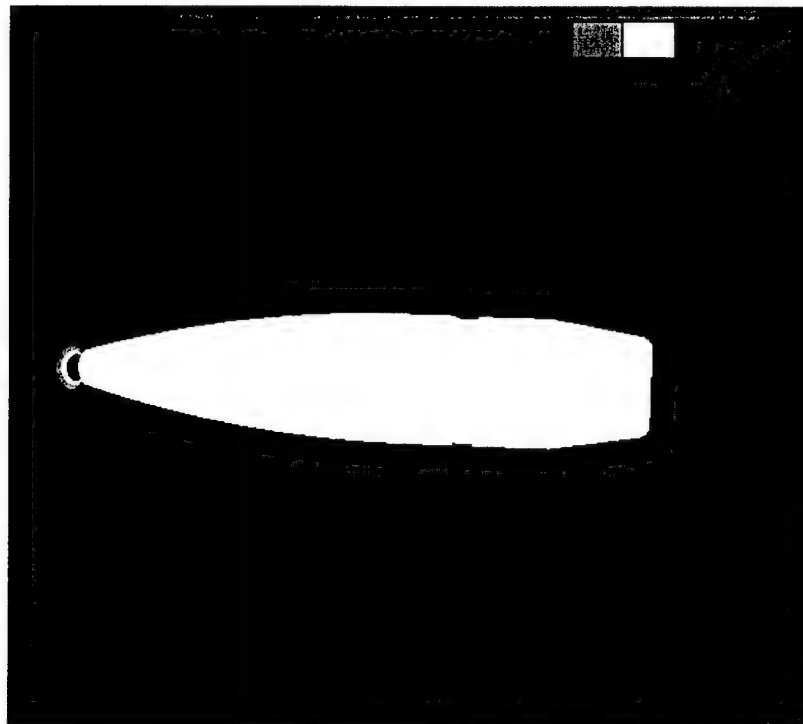


Figure 20. Pressure contours for $M = 0.70$, $\alpha = 2^\circ$, yaw plane.

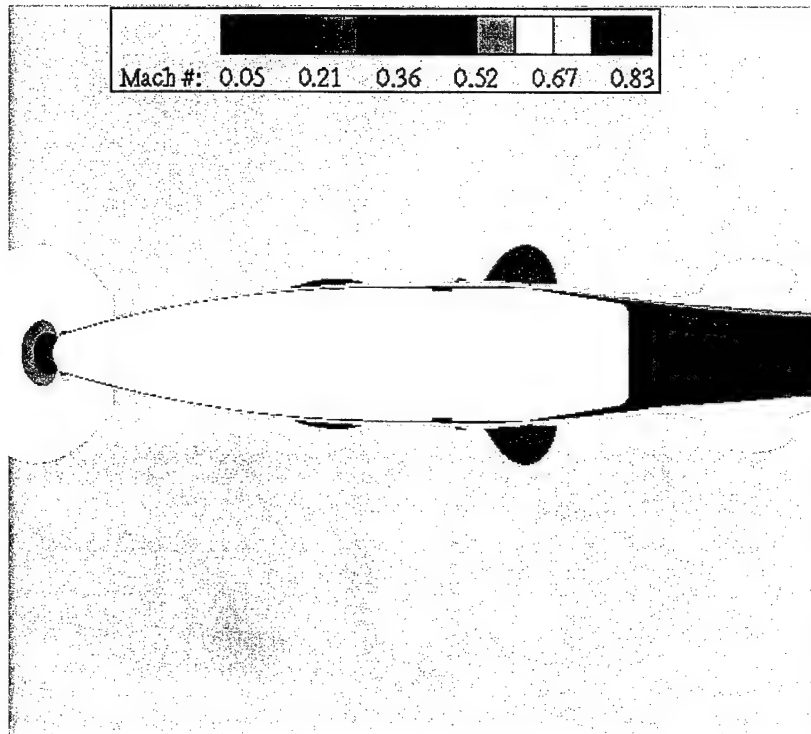


Figure 21. Mach number contours for $M = 0.70$, $\alpha = 2^\circ$, non-yaw plane.

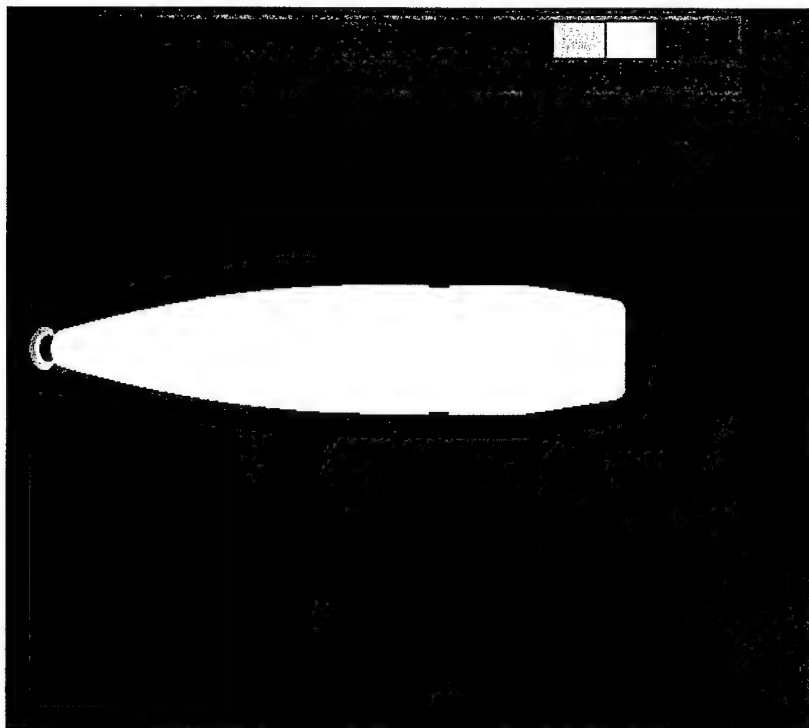


Figure 22. Pressure contours for $M = 0.70$, $\alpha = 2^\circ$, non-yaw plane.

4.3.2 Transonic Flow

The Mach numbers investigated that fall within this category, where the local Mach number may be greater than 1, include Mach 0.85, 0.90, 0.94, and 0.98. The small delta between Mach numbers is due to the rapidly changing flow characteristics in this regime. Although each case is unique, the Mach 0.98 case was the most challenging as indicated by the need for an increase in flow field dimensions in order to properly resolve the flow field. Thus, it is the focus of this section.

As previously mentioned, the far field boundary had to be moved extremely far from the body in order to ensure that it would not interfere with the flow field solution. The main problem with utilizing the grid constructed for the subsonic, other transonic, and low supersonic cases, was that the flow took a great distance to recover from expansion waves and shocks that were created as the flow moved along the body. Once an adequate flow field grid was obtained for the $M = 0.98$ flow, the solution converged fairly quickly. As expected, the flow at $\alpha = 0^\circ$ is axisymmetric. The large expanse of the flow recovery distance is very prominent in the pressure contours of this flow (Figure 23). The blue-green color indicates where approximately free stream pressure is present. One notices the extent of the low pressure regions around the body and the high pressure regions upstream and downstream of the body. The regions take a relatively great distance to recover to nominal free stream pressure. This recovery distance for Mach number (Figure 24) is not as large. Several interesting transonic phenomena still occur, however. The flow becomes slightly supersonic as it expands around the ogive nose and again at the boattail junction. A weak shock occurs at the groove corner. Additionally, a shock occurs prior to the base flow region, as the flow here is nearly stagnant. The region of lower Mach number flow in front of the nose tip is due to the flow anticipating the presence of the body, as the flow is still subsonic.

As would be expected, the flow becomes much more interesting to study at $\alpha = 2^\circ$, if the correct plane is chosen for observation. Beginning with the simplest (i.e., non-yaw) plane, the Mach number contours (Figure 25) remain almost completely symmetric around the body, and the only asymmetry appears to be in the base flow. This is to be expected, as the flow is parallel as it approaches the body in this plane. In the base flow region, the flow is able to mix more with the other planes as the flow separates from the spinning body contributing to the asymmetry. The spinning body contributes to the asymmetry of the pressure in this plane as a Magnus (or side) force is created (Figure 26). This difference in pressure is small, but a slightly higher pressure on the bottom side of the body near the boattail can be seen in the figure. Although the Magnus force is small (and is usually neglected [6]), the Magnus moment is appreciable (Figure 14).

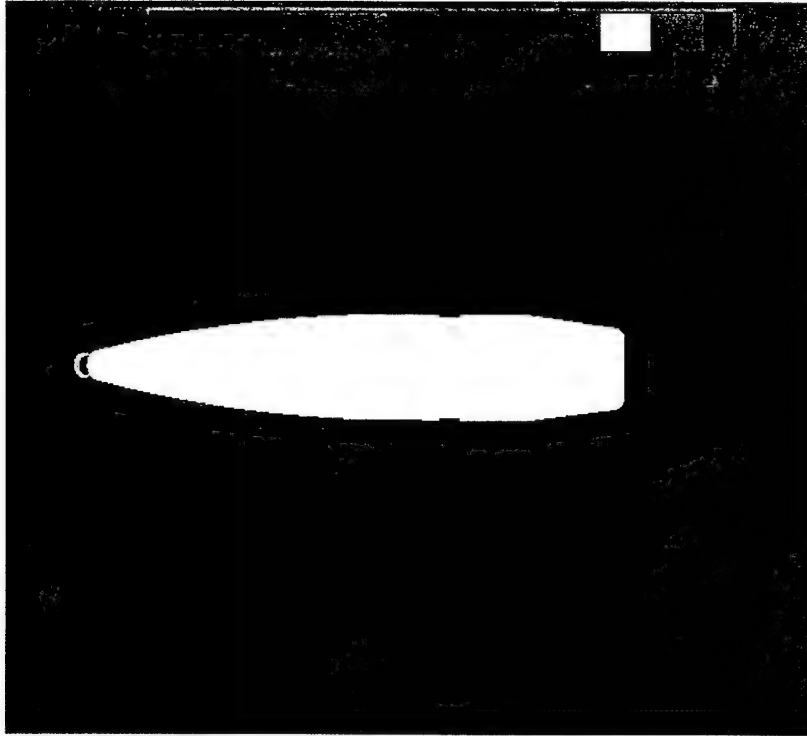


Figure 23. Pressure contours for $M = 0.98$, $\alpha = 0^\circ$, planar cut.

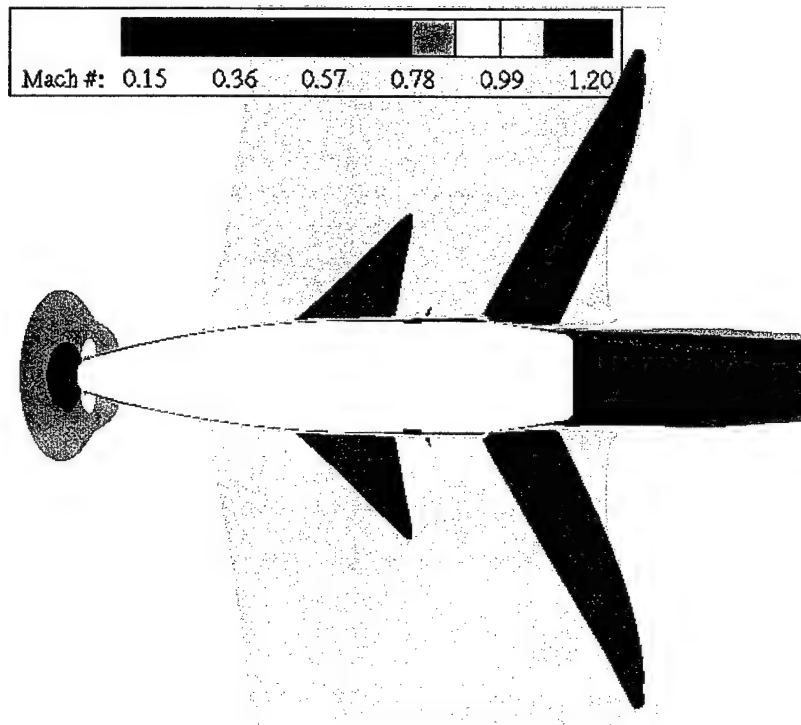


Figure 24. Mach number contours for $M = 0.98$, $\alpha = 0^\circ$, planar cut.

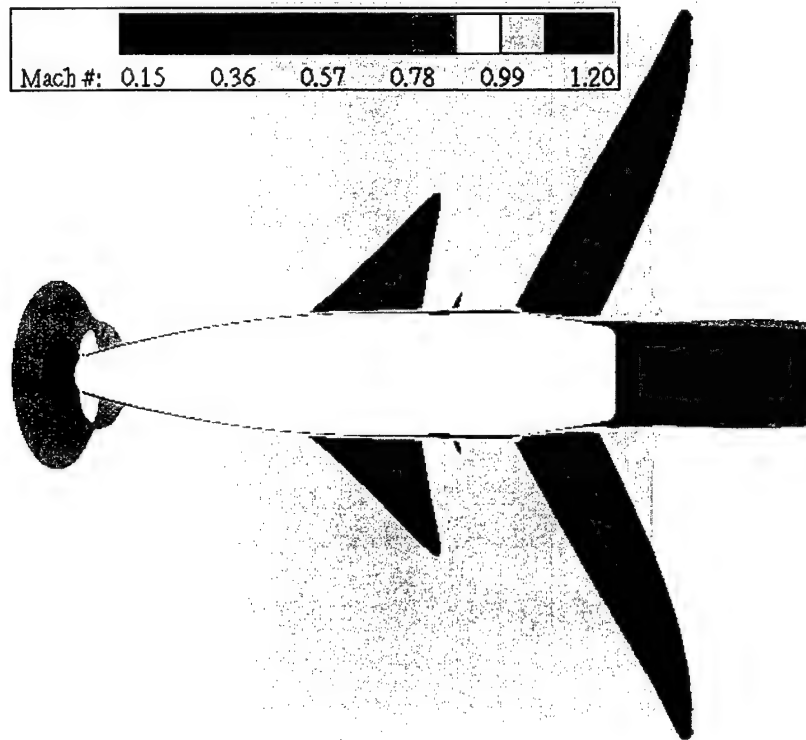


Figure 25. Mach number contours for $M = 0.98$, $\alpha = 2^\circ$, non-yaw plane.

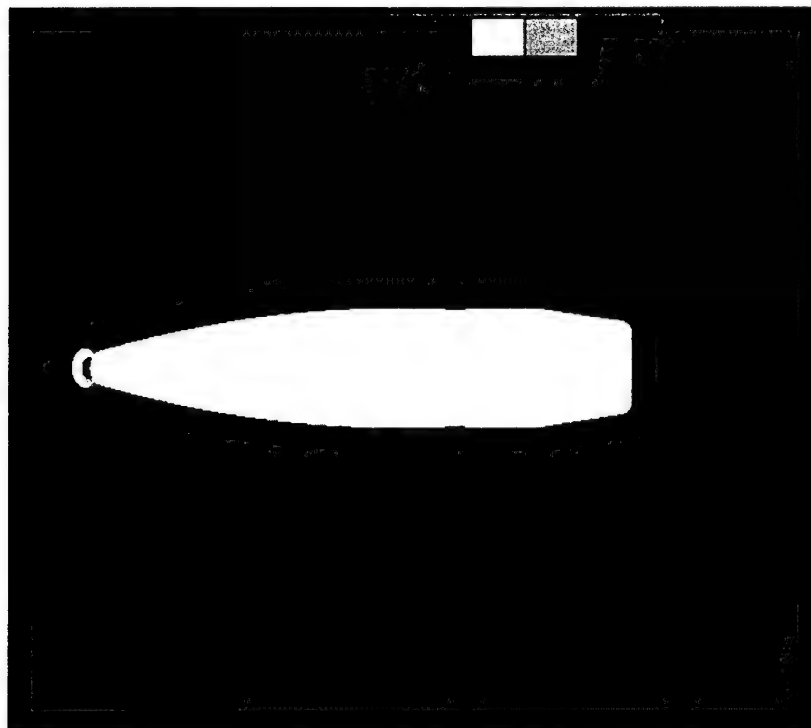


Figure 26. Pressure contours for $M = 0.98$, $\alpha = 2^\circ$, non-yaw plane.

The asymmetries are much more apparent in the yaw angle plane. Many of the features are similar to those of the subsonic case. The first thing that one notices is the nose region where the high pressure region extends further downstream on the windward side of the nose than the leeward side of the nose (Figure 27). The pressure along the main portion of the body is nearly symmetric with only a slightly higher pressure on the windward side of the ogive accounting for the minimum lift being generated for this transonic case (Figure 12). The Mach number contours look very much as expected (Figure 28). The Mach number increases later on the windward side of the nose as the flow takes a greater distance to expand on this side. The larger supersonic Mach number region on the windward side of the boattail is due to the flow having reached the critical Mach number and having to expand through a lesser angle to turn parallel to the body and then back parallel to the flow. These smaller turning angles allow the flow to remain attached longer and a higher Mach number to be achieved.

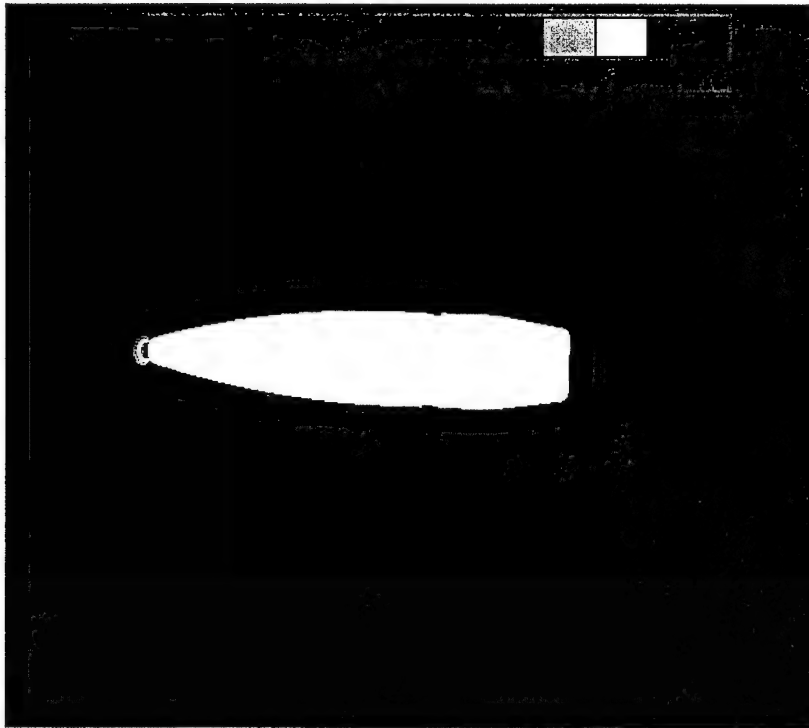


Figure 27. Pressure contours for $M = 0.98$, $\alpha = 2^\circ$, yaw plane.

4.3.3 Supersonic Flow

The supersonic flow cases can easily be separated into two groups: low supersonic (Mach 1.05, 1.10, 1.25) and moderate supersonic (Mach 1.5, 2.0, 2.7). The low supersonic cases are fairly similar in nature and difficulty to the transonic cases and will not be discussed here. The moderate supersonic cases are fairly similar to each other. As such, discussion here will be limited to the Mach 2.0 case.

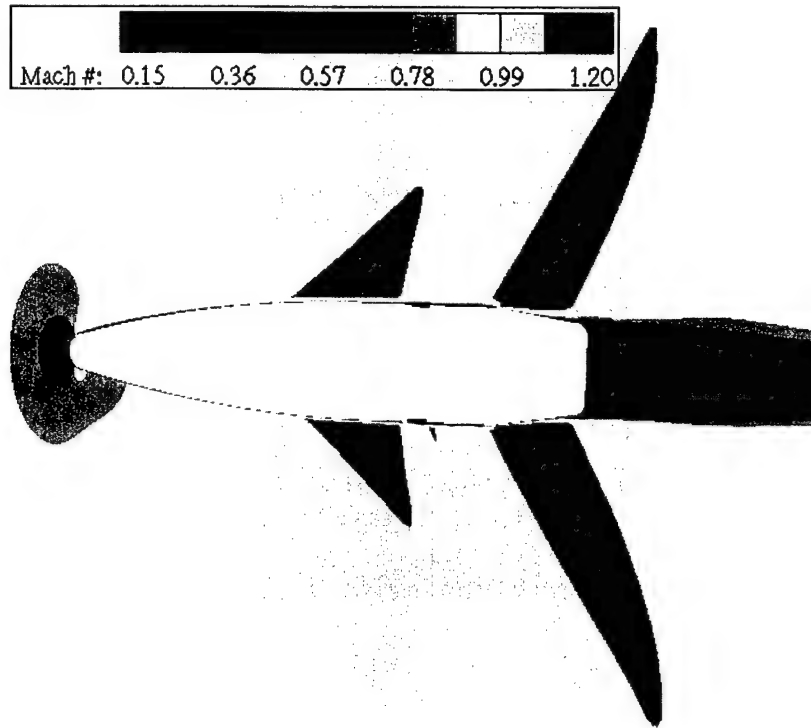


Figure 28. Mach number contours for $M = 0.98$, $\alpha = 2^\circ$, yaw plane.

As with the two previous flow types, the flow at $M = 2.0$, $\alpha = 0^\circ$ is axisymmetric. However, supersonic flow differs from the two previous flow types in that the flow does not anticipate the body. Thus, a curved bow shock exists (Figure 29) so that the flow can be turned parallel to the body. The bow shock also allows the flow to become subsonic along the stagnation streamline so that the velocity can continue to decrease to zero at the stagnation point. The velocity of the flow along the nose and main body is below that of the free stream velocity. The flow does not become subsonic, as the flow is not turned through very large angles. A small shock occurs at the downstream edge of the groove as would be expected of any sharp corner. As the flow expands around the boattail, a region of high supersonic flow develops. A series of weak shocks then form to allow the flow to turn parallel to the free stream as well as meet the base flow region at a shear layer where the pressures match (Figure 30). The region of high pressure is limited to just behind the bow shock. The low-pressure regions are limited solely to area where the flow is expanding: ogive to cylinder, downstream edge of the groove, and around the boattail. In this respect the pressure field is much less responsive to the changes in the flow.

As always, the flow field for the $\alpha = 2^\circ$ configuration is asymmetric. Looking first at the non-yaw angle plane, both the Mach number and pressure contours remain symmetric around the body and only become asymmetric in the base flow regime (Figures 31 and 32). Once again this is due to the flow in this plane being parallel to the body and only in the base flow region does

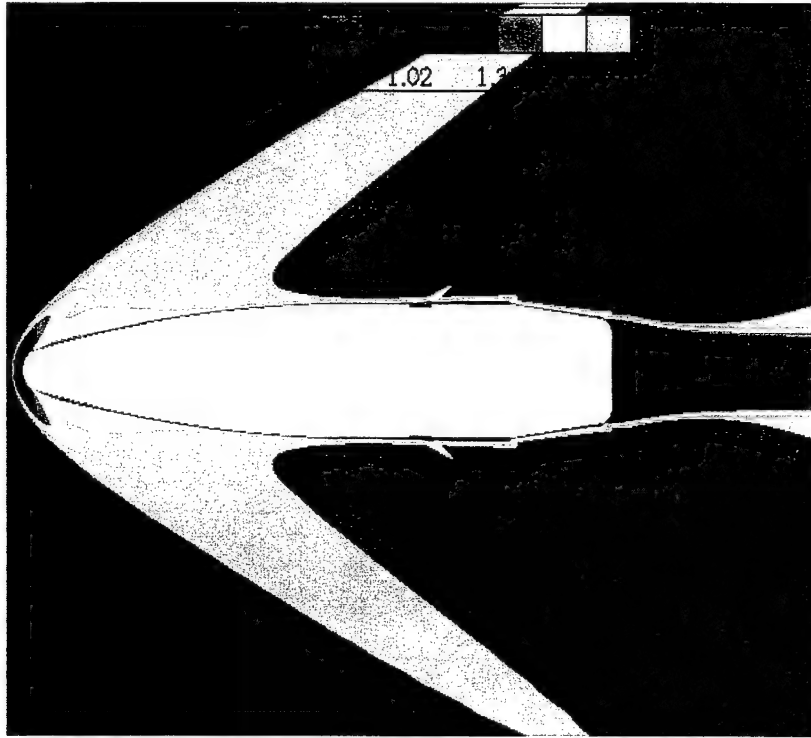


Figure 29. Mach number contours for $M = 2.0$, $\alpha = 0^\circ$, planar cut.

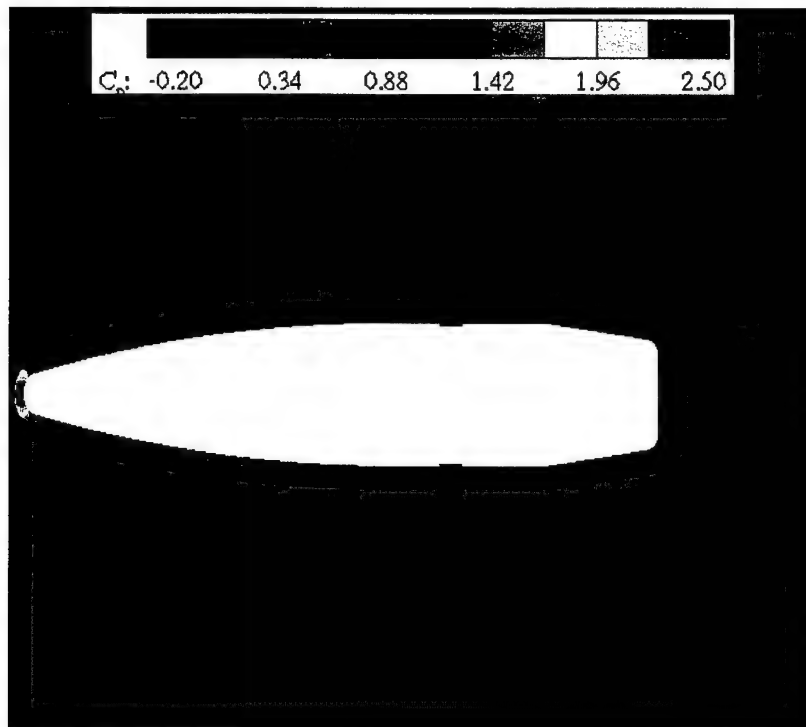


Figure 30. Pressure number contours for $M = 2.0$, $\alpha = 0^\circ$, planar cut.

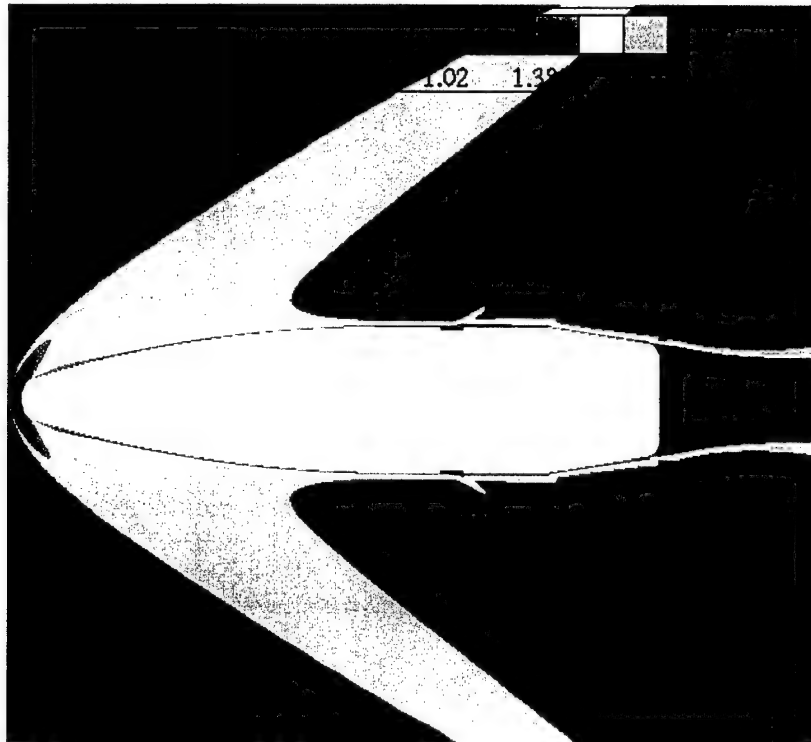


Figure 31. Mach number contours for $M = 2.0$, $\alpha = 2^\circ$, non-yaw plane.

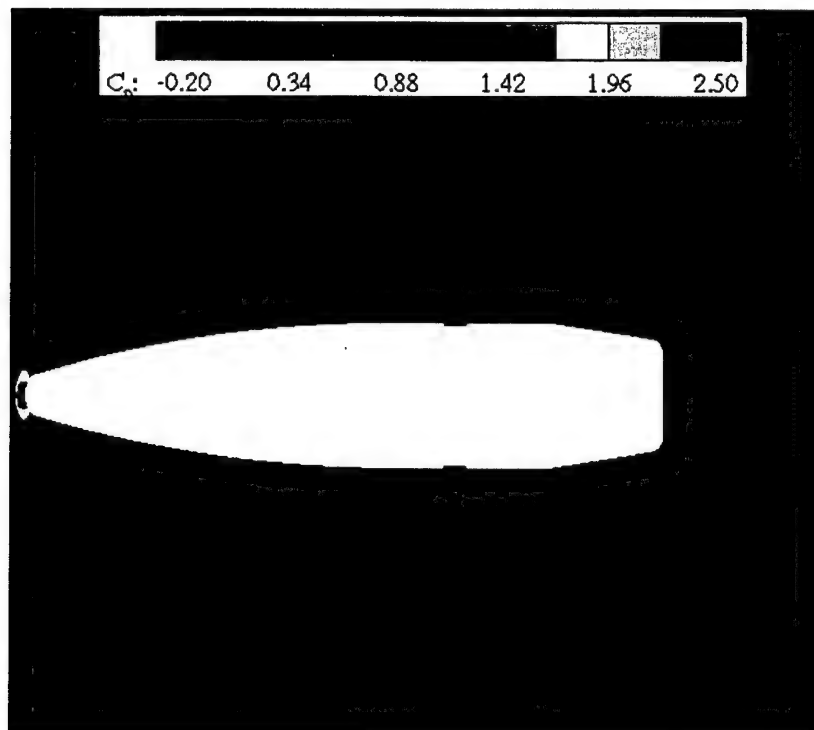


Figure 32. Pressure contours for $M = 2.0$, $\alpha = 2^\circ$, non-yaw plane.

the spinning of the projectile mix the planar flows. The asymmetries are again most noticeable in the yaw angle plane. One first notices the asymmetry of the bow shock, again due to the angle through which the flow must turn in order to remain parallel to the body (Figure 33). The velocity field around the main body remains fairly symmetric, becoming asymmetric as the flow is turned around the boattail. The higher Mach number flow appears to be on the windward side of the body. A larger velocity gradient is also present in this region as the flow turns through shallower angles to have the flow parallel to the boattail and then parallel to the free stream flow. Thus the flow on the leeward side separates earlier. The maximum lift is created at this Mach number (Figure 12) due to the large differential in the low-pressure area on the leeward side and the relatively higher pressure on the windward side (Figure 34). The area of higher pressure on the windward side of the ogive indicates that the nose is probably trying to pitch up. An asymmetry in the pressure field on the base flow is also noticeable for this Mach number.

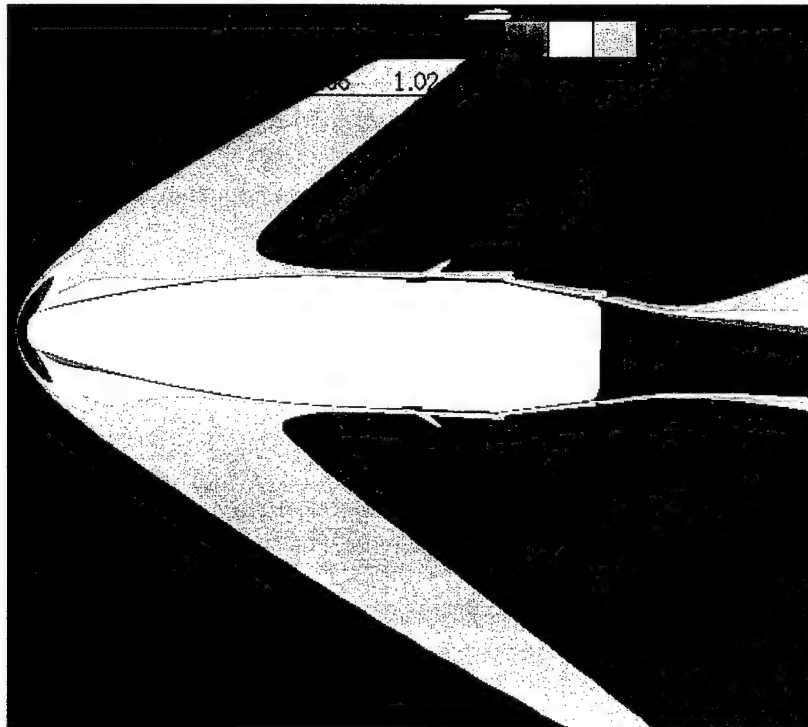


Figure 33. Mach number contours for $M = 2.0$, $\alpha = 2^\circ$, yaw plane.

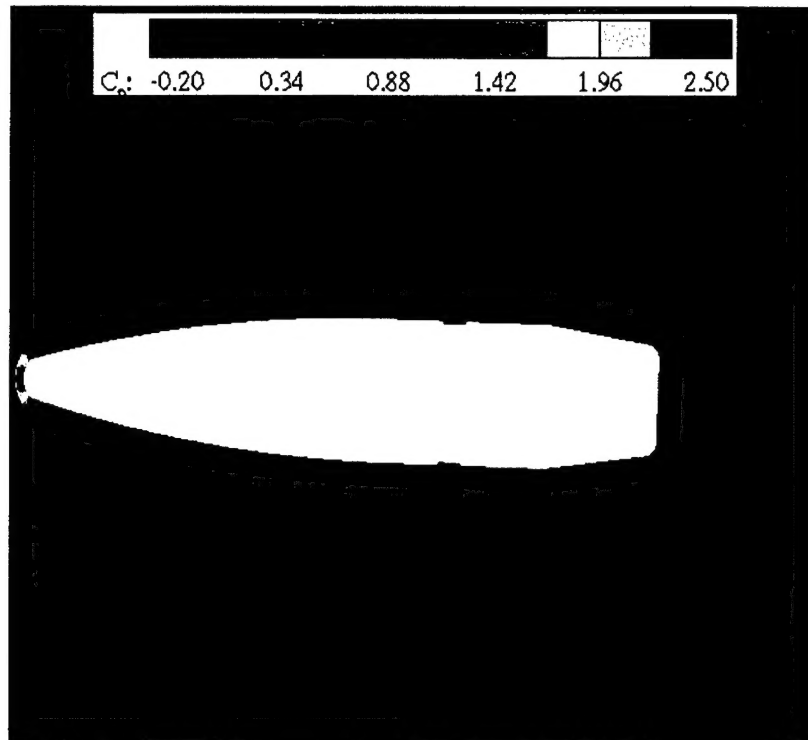


Figure 34. Pressure contours for $M = 2.0$, $\alpha = 2^\circ$, yaw plane.

5. Summary and Conclusions

A computational study has been undertaken to predict the aerodynamic coefficients of a standard spinning projectile using a modern unstructured Navier-Stokes flow solver. Numerical results have been obtained for a wide range of Mach numbers covering the subsonic, transonic, and supersonic flight regimes. Effects of 0° and 2° AOA have been investigated. There is a significant amount of experimental range data available for these cases. Comparison of CFD results to both experimental range data as well as semi-empirical aeroprediction code aerodynamic coefficients shows remarkably good agreement. This agreement shows that CFD is able to provide reasonably good aerodynamic coefficient predictions for spinning projectiles and benchmarks the code for further use in this area of study. Accurate prediction of aerodynamic coefficients also implies that the flow field is being correctly predicted. This allowed for much easier investigation of a projectile of interest to the U.S. Army and a better understanding of flow characteristics.

6. References

1. Sturek, W. B., and L. B. Schiff. "Computations of the Magnus Effect for Slender Bodies in Supersonic Flow." *AIAA Journal*, vol. 20, no. 12, pp. 1724–1731, December 1982.
2. Nietubicz, C. J., W. B. Sturek, and K. R. Heavey. "Computations of Projectile Magnus Effect at Transonic Velocities." BRL-TR-02515, U.S. Army Ballistic Research Laboratory, Aberdeen Proving Ground, MD, August 1983.
3. Sahu, J. "Transonic Navier-Stokes Computations for a Spinning Body of Revolution." BRL-TR-3265, U.S. Army Ballistic Research Laboratory, Aberdeen Proving Ground, MD, September 1991.
4. Sahu, J., K. R. Heavey, and H. L. Edge. "Numerical Computations of Supersonic Flow Over Elliptical Projectiles." ARL-TR-2589, U.S. Army Research Laboratory, Aberdeen Proving Ground, MD, December 2001.
5. Hitchcock, H. P. "Aerodynamic Data for Spinning Projectiles." BRL Report No. 620, U.S. Army Ballistic Research Laboratories, Aberdeen Proving Ground, MD, October 1947.
6. McCoy, R. L. "The Aerodynamic Characteristics of .50 Ball, M33, API, M8, and APIT, M20 Ammunition." BRL-MR-3810, U.S. Army Ballistic Research Laboratory, Aberdeen Proving Ground, MD, January 1990.
7. Guidos, B. J., and S. K. Sung. "Computational Flight Design of .50-Cal. Limited Range Training Ammunition." ARL-TR-662, U.S. Army Research Laboratory, Aberdeen Proving Ground, MD, January 1995.
8. Metacomp Technologies. "CFD++ User's Manual." Westlake Village, CA, 2000.
9. Goldberg, U. C., O. Perroomian, and S. Chakravarthy. "A Wall-Distance-Free K-E Model With Enhanced Near-Wall Treatment." *Journal of Fluids Engineering*, American Society of Mechanical Engineers, vol. 120, pp. 457–462.
10. Aeroprediction Inc. "AP98 User's Guide." King George, VA, 1998.
11. Pointwise Inc. "GRIDGEN User's Manual." Bedford, TX, 1998.
12. FLUENT Inc. "FLUENT 5.0 User's Guide." Vol. 2, Lebanon, NH, 1998.
13. Murphy, C. H. "Free Flight Motion of Symmetric Missiles." BRL Report No. 1193, U.S. Army Ballistic Research Laboratories, Aberdeen Proving Ground, MD, March 1963.

14. Whyte, B. Personal communication. Arrow Tech Corporation, August 2002.
15. Arrow Tech Associates. "ARFDAS 4.1.1 User's Guide." South Burlington, VT, 1997.
16. Kline, R. W., and T. D. Hoffman. "Static and Magnus Aerodynamic Characteristics of the 155-mm M483 Projectile and Its Modifications." TR-4942, Picatinny Arsenal, Dover, NJ, August 1976.

REPORT DOCUMENTATION PAGE			Form Approved OMB No. 0704-0188	
Public reporting burden for this collection of information is estimated to average 1 hour per response, including the time for reviewing instructions, searching existing data sources, gathering and maintaining the data needed, and completing and reviewing the collection of information. Send comments regarding this burden estimate or any other aspect of this collection of information, including suggestions for reducing this burden, to Washington Headquarters Services, Directorate for Information Operations and Reports, 1215 Jefferson Davis Highway, Suite 1204, Arlington, VA 22202-4302, and to the Office of Management and Budget, Paperwork Reduction Project(0704-0188), Washington, DC 20503.				
1. AGENCY USE ONLY (Leave blank)		2. REPORT DATE September 2002		3. REPORT TYPE AND DATES COVERED Final, December 2001-May 2002
4. TITLE AND SUBTITLE Navier-Stokes Computations for a Spinning Projectile From Subsonic to Supersonic Speeds			5. FUNDING NUMBERS 1L1622618.AH80	
6. AUTHOR(S) Sidra I. Silton				
7. PERFORMING ORGANIZATION NAME(S) AND ADDRESS(ES) U.S. Army Research Laboratory ATTN: AMSRL-WM-BC Aberdeen Proving Ground, MD 21005-5066			8. PERFORMING ORGANIZATION REPORT NUMBER ARL-TR-2850	
9. SPONSORING/MONITORING AGENCY NAMES(S) AND ADDRESS(ES)			10. SPONSORING/MONITORING AGENCY REPORT NUMBER	
11. SUPPLEMENTARY NOTES				
12a. DISTRIBUTION/AVAILABILITY STATEMENT Approved for public release; distribution is unlimited.			12b. DISTRIBUTION CODE	
13. ABSTRACT (Maximum 200 words) A computational study has been undertaken to predict the aerodynamic coefficients of a standard spinning projectile using a modern unstructured Navier-Stokes flow solver. Numerical and semi-empirical results have been obtained for a wide range of Mach numbers to include subsonic, transonic, and supersonic flight regimes. Effects of 0°, 2°, and 5° angles of attack have been investigated. Comparison of computational fluid dynamics results to both experimental range data and semi-empirical aeroprediction code results shows remarkably good agreement. Flow field characteristics of each flight regime are explored.				
14. SUBJECT TERMS aerodynamics, Magnus effect, computations, spinning			15. NUMBER OF PAGES 36	
			16. PRICE CODE	
17. SECURITY CLASSIFICATION OF REPORT UNCLASSIFIED	18. SECURITY CLASSIFICATION OF THIS PAGE UNCLASSIFIED	19. SECURITY CLASSIFICATION OF ABSTRACT UNCLASSIFIED	20. LIMITATION OF ABSTRACT UL	